RSC Advances

ROYAL SOCIETY
OF CHEMISTRY

PAPER

View Article Online
View Journal | View Issue

Cite this: *RSC Adv.*, 2025, **15**, 13152

Bacterial responses to *Ephedra aphylla* stem extract and green-synthesized Ag-TiO_2 and Ag-SeO_2 core/shell nanocomposites: unveiling antimicrobial and antioxidant properties†

Mahmood Razzaq Mashar Askar

Received 8th February 2025
Accepted 10th April 2025

DOI: 10.1039/d5ra00936g

rsc.li/rsc-advances

This study reports an efficient and green protocol for the green synthesis of Ag-TiO_2 and Ag-SeO_2 nanocomposites using the extracted stems of *Ephedra aphylla*. Results of spectroscopic and analytical analyses confirmed the successful synthesis, stability, and crystalline nature of the nanomaterials. The phytochemical profile and antioxidant and antimicrobial activities of the *E. aphylla* extract and the nanocomposites were also studied. *E. aphylla* extract and both the nanomaterials exhibited significant levels of active phytochemical compounds. These compounds contributed to their potent antioxidant activity, with *E. aphylla* extract and Ag-TiO_2 NC demonstrating the highest antioxidant activity. Besides, Ag-SeO_2 NC displayed remarkable antibacterial properties against different pathogenic bacteria with 31.0 ± 1.27 mm against *K. pneumonia*, 31.0 ± 1.72 mm against *S. aureus*, and 44.0 ± 1.09 mm against *B. subtilis*, and antifungal properties against *Candida glabrata* and *Aspergillus niger*. The enhanced antimicrobial activity of Ag-SeO_2 NC can be attributed to the synergistic effects of silver and selenium nanoparticles, which can disrupt cell membranes, induce oxidative stress, and interfere with essential cellular processes. The minimum inhibitory concentration values of Ag-SeO_2 NC against *S. aureus* and *K. pneumoniae* were found to be 0.2956 mg mL^{-1} and 4.73 mg mL^{-1}, respectively. The mechanism of action of Ag-SeO_2 NC against both fungal strains was investigated using FTIR and HR-TEM analyses.

1. Introduction

Antibiotic resistance is increasing worldwide along with high mortality caused by new bacteria strains, which drives the necessity to develop novel antimicrobial agents.[1] Traditional medicines use plant extracts containing bioactive compounds because they have been used to treat infections for several years according to scientific research.[2,3] The remarkable antimicrobial activities come from a combination of alkaloids, flavonoids, terpenoids and other related compounds.

Traditional medicines have employed the plant species *Ephedra aphylla* as a medicinal herb for various health purposes for several centuries.[4] Ephedrine and pseudoephedrine along with quercetin, rutin, gallic acid and caffeic acid are bioactive compounds that make this plant a valuable source.[5–7] The increasing importance of *E. aphylla* as an herbal pharmaceutical plant derives from its utility in providing natural bioactive substances that demonstrate multiple pharmaceutical effects.[8] Recent studies focus on the development of metal and metal oxide nanoparticles through eco-friendly plant extract methods.[9]

Nanomaterials present distinct physico-chemical behavior that scientists find useful in antimicrobial studies.[10] Many scientists prefer metal and metal oxide nanoparticles as antimicrobial agents owing to their excellent reactivity levels, high surface area properties and proven action against microbes.[11] As these materials exhibit adverse effects on the environment and toxicity issues, scientists have developed plant extract-based natural synthesis procedures as an alternative solution.[12] When nanoparticles release silver ions, they show lethal effects against bacteria by disrupting several bacterial processes.[13–15] When exposed to the visible light spectrum, the photocatalytic activity of TiO_2 is initiated to produce ROS, which include hydroxyl and oxygen radicals.[16] ROS particles created *via* visible light exposure degrade the bacterial cell wall and membrane until the microorganisms become inactive.[17] Nanoparticles have the capability to penetrate bacterial cell walls and establish direct interactions, resulting in cell damage that leads to bacterial death.[18]

Research conducted by multiple investigators in recent times has proven that Ag-TiO_2 and Ag-SeO_2 nanocomposites show strong antibacterial effects against various bacterial strains.[13–15] Research conducted by scientists established that

---

Department of Special Education Sciences, Imam Alkadhim University College, Iraq. E-mail: Lecdhi118@iku.edu.iq; mahmoodaskar78@gmail.com

† Electronic supplementary information (ESI) available. See DOI: **https://doi.org/10.1039/d5ra00936g**

nanomaterials incorporating Ag-TiO_2 and Ag-SeO_2 demonstrated powerful antibacterial effects on Gram-positive and Gram-negative bacteria along with *E. coli*, *S. aureus*, and *P. aeruginosa*[19] while showing effective antifungal properties against fungal microorganisms.[20]

Different industries can utilize Ag-TiO_2 and Ag-SeO_2 nanocomposites owing to their wide array of potential applications. Nanomaterials show promise as water decontamination agents that eliminate bacterial and viral microorganisms.[21,22] Nanocomposite particles improve food packaging materials while maintaining product stability and preventing the transmission of contagious diseases in foods.[23] These nanocomposites enable medical professionals to create antimicrobial surface coatings for medical tools that defend against patient infections.[24] Ag-TiO_2 NC integration with textiles allows fabric development to block bacterial growth, including odor-causing bacteria.[25] The assessment of the long-term safety and environmental sustainability of Ag-TiO_2 NCs requires further research. Sustainable and eco-friendly nanocomposite production through green synthesis provides a dual protection mechanism against antibiotic resistance while improving human wellness.

AgNPs (silver nanoparticles), TiO_2 NPs (titanium dioxide nanoparticles) and SeNPs (selenium nanoparticles) demonstrate antimicrobial properties because they damage membranes and produce reactive oxygen species (ROS), which disrupt metabolic activities. Bacterial death results from AgNP activity owing to Ag^+ ion production, which breaks both the membrane structure and protein formation within pathogens.[26] Research has shown that AgNPs can be used for wastewater treatment because they successfully prevent microorganisms from multiplying.[27] TiO_2 NPs release ROS under both UV illumination conditions that destroy microbial cells, thus making them effective agents against plant pathogens, including *Alternaria alternata*.[28] The combination of Ag or Se with TiO_2 surfaces serves as an effective method for bacterial inhibition and enhances osteoblastic cell growth, which makes these materials suitable for biomedical device applications.[29] SeNPs, which are less toxic than AgNPs, are metabolic inhibitors that can inhibit bacterial growth, biofilm formation, and foodborne bacteria.[30,31] Their potential use as antimicrobial agents in chitosan solutions has been demonstrated in recent studies, suggesting dental and wound healing applications.[32] The synergistic action of employing Ag and Se nanoparticles combined on Ti surfaces has been documented to enhance antimicrobial action. These observations indicate that nanoparticle blends might strengthen microbial defense mechanisms and could be exploited in medicine, agriculture, and food security applications.[28,29]

Ag-TiO_2 NC proved effective because TiO_2 demonstrates known photocatalytic capabilities to generate reactive oxygen species (ROS) under light, which enhances antimicrobial sterilization.[33] The combination of Ag NPs with TiO_2 produces enhanced antibacterial and antioxidant properties, which makes the material suitable for various biomedical applications, water purification systems, and antimicrobial packaging needs.[34] Ag-SeO_2 NC shows promise because selenium plays a vital biological role in cell metabolic processes and demonstrates antimicrobial behavior at lower toxic levels than other heavy metals.[35] Ag-SeO_2 NC was reported to verify enhanced microbial suppression through membrane-bursting activity along with the production of oxidative stress during bacterial dysfunction and cellular function blockade.[36] The pharmaceutical and biomedical industries require such materials to meet their requirements of both antimicrobial breadth and biological compatibility. *Ephedra aphylla* extract enabled the first-time green synthesis of Ag-TiO_2 and Ag-SeO_2 NCs by enabling both stability improvement and bioactivity enhancement of the nanocomposites through their phytochemical properties.

The main goal of this work is to establish an efficient and green protocol for the preparation of Ag-TiO_2 and Ag-SeO_2 nanocomposites using the stem extract of *E. aphylla*. This novel green synthesis method also eliminates the further use of dangerous chemicals and toxic solvents, which lowers the environmental drawbacks of nanomaterial production and processing. Furthermore, this study employs different techniques to determine the properties of the synthesized nanocomposites, assess their antimicrobial and antioxidant properties, and determine the mode of action and possible uses of nanocomposites in diverse areas of application. The improved antimicrobial activity of the nanomaterials produced can be attributed to the synergistic interaction between silver and selenium NPs and their interaction with bacterial cell membranes and different intracellular targets that lead to cell death.

2. Materials and methods

2.1. Reagents

The reagents used in the study were of analytical grade (for details, see the ESI file, Section S1†).

2.2. Instruments

UV-visible spectroscopy was employed using a Spectrophotometer UV2 (Uni-cam UV-vis, USA). Fourier Transform Infrared (FTIR) spectroscopy (Thermo-Fisher Nicolet IS10, USA) was used to identify functional groups with a resolution of 4 cm^{-1} across a wavenumber range of 500–4000 cm^{-1}. The surface charge of the nanoparticles was determined using zeta potential analysis (HORIBA SZ-100). High-resolution-transmission electron microscopy (HR-TEM) analysis (Thermoscientific, Talos F200i) provided insights into the size, shape, aggregation behavior, and crystallinity of nanoparticles. Scanning electron microscopy (SEM) equipped with energy-dispersive X-ray (EDX) spectroscopy was employed to investigate the surface features, morphology, and elemental composition. This analysis was performed using a Czech FEI-type SEM instrument at an accelerating voltage of 25 kV. X-ray diffraction (XRD) analysis using a Panalytical Philips instrument helped determine the crystal structure of the nanomaterials. A spectrophotometer (Spekol 11, Analytik Jena AG, Jena, Germany) was employed to assess the antioxidant and phytochemical profiles.

2.3. Preparation of *E. aphylla* extract

E. aphylla stems were collected from further banks of the Tigris and Euphrates rivers. The collected stems were washed with cold water, dried with the help of paper towels, and left to dry for a few hours. Alhammadi (2012) used 20 grams of dried plant material to prepare 100 mL of 70% ethanol, which was macerated at 30 °C for 24 hours with a view to making bioactive compounds more soluble. The mass was subsequently filtered through Whatman no 1 filter paper and further subjected to centrifugation for 15 minutes at 15 000 rpm for further pellet removal. The purified extract was used immediately for nanocomposite solutions and other analysis and application-related studies.[8,37]

2.4. Green synthesis of nanocomposites

A plant-mediated green synthesis technique[38–40] was employed to prepare nanocomposites using the ethanol extract of *E. aphylla*. Silver-selenium dioxide nanoparticles were prepared using (25 mL, 1 mM) silver nitrate solution and the prepared extract. A solution container included selenium dioxide (50 mg in 10 mL ethanol) besides titanium dioxide (50 mg in 10 mL ethanol). The solutions underwent sonication treatment at 30 ° C for 15 minutes. The researchers mixed 1 mM silver nanoparticle solution (25 mL) with sonicated titanium dioxide solution under 30 °C continuous stirring for 15 minutes to prepare a silver-titanium dioxide nanocomposite. A combined mixing of silver nanoparticle solution with appropriate selenium dioxide solution continued while being stirred for 15 minutes at a temperature of 30 °C. Both Ag-TiO_2 and Ag-SeO_2 NC solutions underwent heat treatment at 60 °C while maintaining continuous stirring for 5 hours before subjecting them to 2 hours of sonication at 60 °C. A spectrophotometer helped confirm the formation of nanoparticles by observing the color transformations. Ag-TiO_2 NC solution underwent dark yellow to dark green color transformation, while Ag-SeO_2 NC progressed from pale yellow to dark brown coloration. The extraction of nanoparticles took place through centrifugation at 15 000 rpm for 20 minutes using each solution. A washing routine involving distilled water, followed by ethanol, purified the solid nanoparticles from their contaminants. The dry process was finished by placing the solid nanoparticles in an oven heated to 60 °C. The researchers preserved part of the solution at −70 °C in dark storage to prevent the degradation of solution constituents.[38]

2.5. Phytochemical analysis

Analysis of the plant extract and nanocomposites involved the identification of their phytochemical profiles together with antioxidant activity assessment. The analysis of phenolic content used the Folin–Ciocalteu (F–C) assay[41] and flavonoid content evaluation, followed by the aluminum chloride assay.[42] The tannin content in the samples was evaluated *via* a vanillin–hydrochloride reaction method.[43] The research data analysis utilized a gallic acid standard curve relationship with $y = 0.0062x$ and $R^2 = 0.987$ and obtained results as mg g^{-1} of dry sample. The evaluation of the flavonoid and tannin content in extracts used catechin as a standard to develop the calibration curve ($y = 0.0028x$, $R^2 = 0.988$) as well as tannic acid ($y = 0.0009x$, $R^2 = 0.955$). A supplemental file contains complete procedures for conducting phytochemical tests.

2.6. Biological assessment

2.6.1. Antioxidant activity evaluation. The 2,2-diphenyl-1-picrylhydrazyl (DPPH) radical scavenging assay tested the antioxidant properties of all the collected samples.[44] The investigators prepared a DPPH solution from methanol at a concentration of 0.25 mg mL^{-1} before preparing diluted aliquots of the samples through the methanol solution. During the 30 minutes incubation at room temperature, the researchers conducted a mixing procedure that combined one milliliter of DPPH solution with tubes containing the solution dilutions. During the experiment, the spectrophotometer measured the reaction mixture absorbance values at a wavelength of 517 nm. The percentage computation of DPPH radical inhibition was evaluated using the following expression:

$$\text{Inhibition (\%)} = [(A\text{“control”} - A\text{“sample”})/A\text{“control”}] \times 100,$$

where A“control” is the absorbance of the control (without the test material) and A“sample” is the absorbance of the sample mixture. Higher inhibition percentages indicate stronger antioxidant activity, reflecting a greater ability to reduce the DPPH radical. The IC_{50} values, representing the concentration required to inhibit 50% of the DPPH radical, were determined from an exponential curve correlating the sample concentration with the remaining percentage of DPPH. Lower IC_{50} values indicate a higher antioxidant capacity.[45]

2.6.2. Microbial susceptibility testing

2.6.2.1. Antibacterial activity assessment. The antimicrobial activity of the samples was evaluated using an agar well diffusion assay. Distilled water served as a negative control, while gentamicin, a standard antibiotic, was used as a positive control. Mueller–Hinton agar plates were prepared according to standard protocols.[46] The bacterial inoculum was evenly spread across the agar plate using a sterile swab to create a bacterial lawn. A sterile cork borer was used to create a well in the center of the agar plate, approximately 6 mm in diameter and 5 mm deep. Each sample solution (100 μL) was carefully pipetted into the well. The agar plates were incubated at 37 °C for 24 hours to allow for bacterial growth and inhibition by the samples. The diameter of the clear zone of inhibition surrounding the well was measured, indicating the antimicrobial activity of the sample. Larger zones of inhibition signify greater antimicrobial potency.

2.6.2.2. Broth microdilution assay. To determine the MIC of the sample against *S. aureus* and *K. pneumoniae*, serial dilutions were prepared in nutrient broth medium at concentrations ranging from 16.58 to 0.0324 mg mL^{-1} for Ag-TiO_2 NC and from 9.46 to 0.0185 mg mL^{-1} for Ag-SeO_2 NC. A control containing only inoculated broth was incubated for 24 hours at 37 °C. The MIC was identified as the lowest concentration at which no visible bacterial growth was observed in the tubes. The turbidity of the tubes was visually assessed before and after incubation to confirm the MIC value, and the optical density (OD) was measured at 600 nm for further verification.[47]

2.6.2.3. Antifungal activity assessment. To assess the antifungal activity of the plant extract and nanocomposites against *Candida glabrata* and *Aspergillus niger*, a disc diffusion assay was employed.[48] Sterile filter paper discs were impregnated with 10 μL of the plant extract, nanocomposite solution, standard antifungal drug (fluconazole), or sterile distilled water (negative control). The researchers set the fungal culture on agar plates before adding the prepared discs. After placing the plates into an incubator at 37 °C, they remained there for 24–48 hours. The antifungal activity determination involved measuring the clear zone diameter that formed around each disc following the incubation period. A larger zone of inhibition shows an increased antifungal capacity of the applied substances.

2.7. Statistical analysis

The results are presented as mean values ± standard deviation (SD). All experimental phytochemical analyses and antibacterial assessments of the *Ephedra aphylla* extract and the synthesized nanocomposites were conducted in triplicate. The Statistical Package for Social Sciences (SPSS, version 21) provided an evaluation of the mean values obtained from the samples. A one-way analysis of variance (ANOVA) provided statistical analyses, and differences at or below $p \leq 0.05$ were considered significant.

3. Results and discussion

3.1. Plausible mechanism for the formation of nanocomposites

The chemical reaction process for green nanocomposite synthesis uses *E. aphylla* extract to perform various stages of the synthetic procedure. An explanation of the Ag-TiO_2 and Ag-SeO_2 NC green synthesis with *E. aphylla* extract follows in this section, as displayed in Fig. 1. *E. aphylla* goes through two processes to extract ethanol-based bioactive compounds: polyphenols and flavonoids together with tannins. Silver nitrate is then dissociated in the solution to generate silver ions (Ag^+) and nitrate ions (NO_3^-). The phytochemical compounds donate electrons to the Ag^+ ions, resulting in the bioreduction, nucleation, and growth of silver nanoparticles.[49] Subsequently, the silver nanoparticles interact with TiO_2 or SeO_2 nanoparticles, resulting in the formation of Ag-TiO_2 or Ag-SeO_2 nanocomposites.[13] The interactions of silver nanoparticles with metal oxides, such as TiO_2 or SeO_2, can cause several changes in the characteristics of the final solution. First, it can alter the position of the SPR of the silver nanoparticles, meaning that it alters the absorption and scattering properties of light as well as the color of the solution.[50] Second, charge transfer processes are possible at the interface between silver nanoparticles and metal oxide, affecting the electronic structure of the nanoparticles and their plasmonic response.[51] Finally, the adsorption process of Ag nanoparticles on the surface of the formed metal oxide (TiO_2 or SeO_2) nanoparticles alters the optical characteristics of the solution, leading to the formation of Ag-TiO_2 or Ag-SeO_2 nanocomposites.[52]

The synthesis of nanoparticles through plant extracts depends on bioactive molecules, such as phenolics, flavonoids, and tannins, along with proteins, terpenoids, and polysaccharides that function as reducing and stabilizing agents. Metal ion reduction occurs through phenolics and flavonoids, resulting in smaller nanoparticles, but tannins provide stability improvements.[53] Enzymes and proteins accelerate reduction while enhancing crystallinity, but terpenoids along with polysaccharides inhibit agglomeration and adjust surface charge levels.[54] The concentration of biochemical compounds influences nanoparticle size together with their shape characteristics and stability because flavonoid-containing extracts create spherical shapes, while tannin extract solutions develop non-spherical structures.[55] The effectiveness of reduction agents leads to higher crystallinity, and surface charge control stems from capping agents, which stabilize dispersion.[56] Laboratory control of nanoparticle fabrication methods becomes possible through a comprehensive understanding of the synthesis mechanisms, which leads to numerous practical applications in medicine, catalysis, and environmental remediation.

In addition, the stability and antimicrobial properties of nanocomposites strongly respond to environmental conditions, including pH and temperature measurements. When pH values change, they affect nanoparticle dispersion factors and surface charge distribution, which determine the rate of ion release and aggregation patterns.[57] Silver-based nanocomposites leverage acidic solutions to increase Ag^+ ion release, which drives up their antimicrobial effects, but alkaline conditions result in reduced ion release, which lowers their effectiveness.[58] Temperature functions as an essential determinant that influences the synthesis processes of both nanocomposites while affecting their stability throughout their existence. Synthesis of proper nanoparticles occurs when heating is controlled at 60 °C for five continuous hours. The prolonged existence of high-temperature conditions causes nanoparticle aggregation along with oxidation, which pulls down their stability and biological effectiveness.[59] The nanocomposites remain stable when they are preserved at −70 °C under dark conditions, which protects their structure together with their antimicrobial properties. The long-term usage and effectiveness of nanocomposites in biomedical and environmental areas require exact pH and temperature management.

3.2. Characterization of nanocomposites

3.2.1. UV-visible spectroscopy. UV-visible spectroscopy was employed to investigate the optical properties of the synthesized nanocomposites (Fig. 2a). The absorbance spectra of the *E. aphylla* extract and the synthesized Ag-TiO_2 and Ag-SeO_2 NCs were recorded at various wavelengths. The *E. aphylla* extract demonstrated a major absorbance maximum at 468 nm that scientists related to its bioactive compounds, with alkaloids and flavonoids showing distinct absorption properties. The absorbance peak at 468 nm results from $n \rightarrow \pi^*$ transitions in compounds that have chromophores containing non-bonding electrons found in carbonyl groups (C=O) and aromatic rings with heteroatomic lone pairs (*e.g.*, nitrogen or oxygen).[60] The

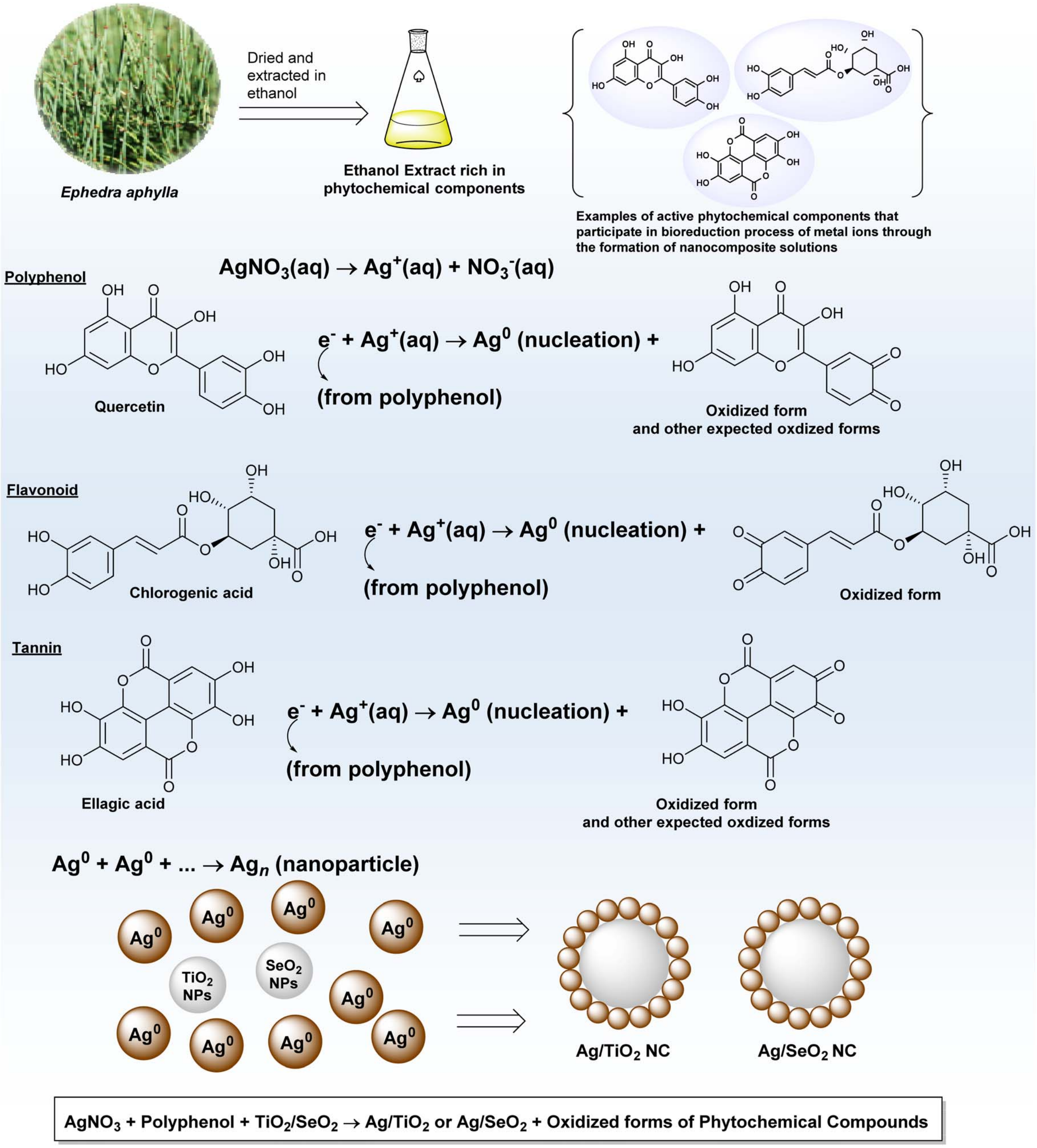

Fig. 1 Proposed mechanism of formation of Ag-TiO_2 and Ag-SeO_2 NCs.

color manifestation occurs from transitions observed in the visible spectrum owing to chemical processes. The specific absorbance of Ag-TiO_2 nanomaterials appeared at 562 nm owing to their silver nanoparticle-specific surface plasmon resonance characteristics.[61] The SPR band red shift from silver bulk to silver nanoparticles demonstrates the existence of large-sized silver nanoparticles.[62]

The Ag-SeO_2 nanomaterial showed its absorbance peak at 480 nm, and this observation could be explained by the SPR of the silver nanoparticles (Fig. 2a). The wavelength position shifts toward the red region of the silver spectrum along with its observation, indicating that moderate-sized silver nanoparticles can be formed. The placement of SPR bands in nanoparticles depends on factors that incorporate their physical dimensions together with their shapes and dielectric composition.[61] The optical properties of the composite materials could be affected by TiO_2 and SeO_2 when combined with the materials, possibly influencing light scattering along with electronic transitions. The UV-visible spectroscopy data show the verification of nanomaterial synthesis when silver-based nanomaterials show different detectable optical characteristics. The absorbance peaks demonstrate that silver nanoparticles exist in the sample with TiO_2 and SeO_2 semiconductor components.

3.2.2. FTIR spectral analysis.

Spectral analysis using FTIR on the *E. aphylla* extract is presented in Fig. 2b, with the identification of different functional groups illustrated in Table S1.†

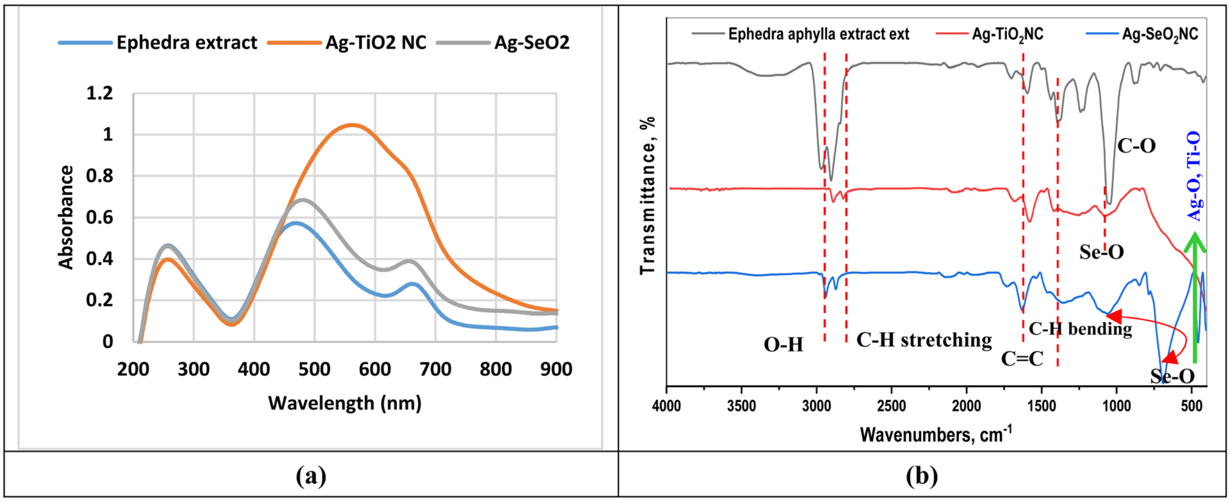

Fig. 2 Spectral analysis of the plant extract and nanocomposites: (a) UV-visible spectra and (b) FTIR spectra of *Ephedra aphylla* extract (23.98 mg mL^{-1}), Ag-TiO_2 NC (33.16 mg mL^{-1}), and Ag-SeO_2 NC (18.92 mg mL^{-1}).

Hydroxyl functional groups appear in the spectrum as a wide peak at 3550 and 3540 cm^{-1} through O–H stretching patterns, which occur in alcohol compounds and certain phenol and carboxylic acid systems. The FTIR spectrum section four displays stretching frequencies of aliphatic compound C–H, which appear at 2989, 2965, 2915, and 2848 cm^{-1}. As detection markers for these groups within the sample, the carbonyl C=O stretching bond (1709 cm^{-1}) is accompanied by the aromatic vinyl C=C stretch (1601 cm^{-1}).

The peaks found at 1078, 1044, 897, 868, 762, and 718 cm^{-1} show C–O stretching vibrations, which indicate the presence of compounds, including alcohols and ethers together with esters. Several characteristic absorption bands appeared in the FTIR spectrum of the Ag-TiO_2 NC (Fig. 2b). The C–H stretching vibrations appear at 2913 and 2845 cm^{-1}, demonstrating the persisting organic materials introduced by the plant extract in the synthesis process. The Ti–O–Ti stretching bonds appear at 1105 cm^{-1} in the spectrum, which indicates that the TiO_2 phase exists within the sample structure.[63] Vibrations at 414 and 378 cm^{-1} correspond to metal–oxygen bonds, which most probably involve Ti–O and Ag–O bonding patterns, respectively.[64] The main bands in the spectrum indicate the successful creation of Ag-TiO_2 NC by combining TiO_2 and silver nanoparticles. The synthesis process of nanomaterials was aided by plant extract residual compounds that simultaneously played the roles of reducers and surface stabilizers.[65]

The FTIR spectrum of Ag-SeO_2 NC displayed various distinct peak bands. The FTIR spectrum shows two peaks at 2914 and 2846 cm^{-1} from the C–H stretching vibrations because the spectrum contains residual organic compounds from the plant extract. The FTIR spectrum exhibits Se–O and Ag–O bond vibrations through the various bands present at 1731, 1604, 1507, 1442, 1104, 1034, 822, 762, 709, 665, 490, 430, and 378 cm^{-1}.[66] Ag-SeO_2 NC formation was successful because of the absorption bands observed in the spectrum. Ag-TiO_2 NC produced a significantly weakened biomolecule peak intensity in its spectral analysis. The biomolecules from the extract participated during synthesis by reducing metal ions and serving to stabilize them. New peaks indicating Ti–O–Ti bond formation and metal–oxygen bond formation identify the production of Ag-TiO_2 NC. An intensity decrease in the biomolecular peaks appears in the spectrum of Ag-SeO_2 NC. New peaks indicating Se–O together with Ag–O bonds appear in the spectrum to verify the synthesis of Ag-SeO_2 NC.[67] The FTIR examination provides compelling proof that biomolecules from *E. aphylla* extract take part in the green nanomaterial formation method of Ag-TiO_2 and Ag-SeO_2. Analysis through FTIR showed that new peaks linked to metal–oxygen bonds in combination with vanished functional groups proved that the nanocomposite synthesis was successful.

3.2.3. Zeta potential.

The zeta potential data measured surface charge and stability levels of Ag-TiO_2 and Ag-SeO_2 nanocomposites, as depicted in Fig. 3a, b and S2.† The zeta potential measurements of both nanomaterials yielded negative results, indicating that anionic particles exist in the test solutions. Electrostatic charges emerge on extra surface components because of hydroxyl functional groups, which enable proton release until the particle surface exhibits a negatively charged field.[68] The numerical value of zeta potential is measured in mV and systems maintain better stability because of robust electrostatic repulsive forces between particles that prevent aggregation.[69] In this case, both Ag-TiO_2 and Ag-SeO_2 nanoparticles show relatively high negative zeta potentials, indicating that the dispersion stability of the nanoparticles in aqueous media is generally favorable. Nevertheless, the Ag-TiO_2 nanoparticles have approximately a neutral charge (−32.4 mV) (Fig. 3a), showing slightly better stability than the Ag-SeO_2 nanoparticles (−29.2 mV) (Fig. 3b). These variations in zeta potential could be due to differences in surface charge, particle, size, and synthesis conditions.[70] Altogether, the results of the zeta potential in the present study confirm that both Ag-TiO_2 and Ag-SeO_2 nanomaterials have reasonable colloidal stability.

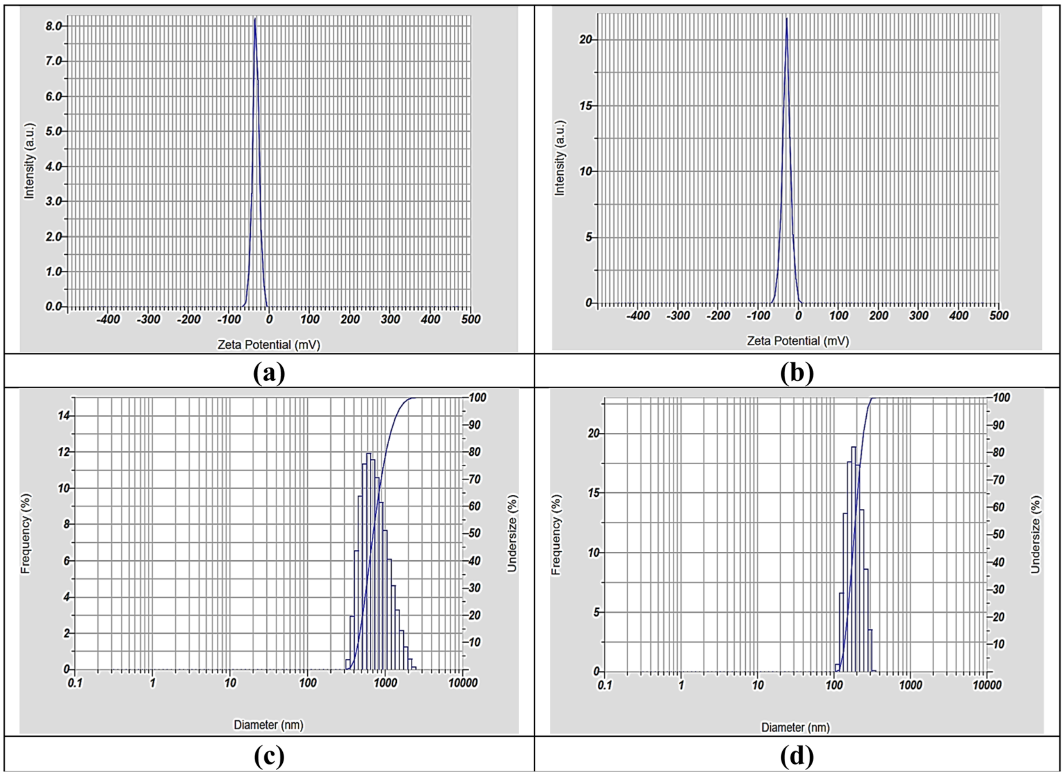

Fig. 3 Zeta potential and DLS analysis: (a) zeta potential of Ag-TiO_2 NC and (b) Ag-SeO_2 NC. (c) DLS of Ag-TiO_2 NC and (d) Ag-SeO_2 NC.

Nonetheless, the slightly higher zeta potential of Ag-TiO_2 nanoparticles suggests that these nanoparticles may offer slightly better stability in aqueous dispersion over a longer term.

3.2.4. Dynamic light scattering (DLS). Particle size analysis of the prepared Ag-TiO_2 and Ag-SeO_2 NCs was performed through DLS and is presented in Fig. 3c, d, S3 and S4.† In the case of Ag-TiO_2, the zeta average measured 795.5 nm, and PDI 0.410 (Fig. 3c), hence suggesting large agglomeration potential with a size distribution spread. However, Ag-SeO_2 NC had an average zeta of 191.0 nm and a PDI of 0.132 (Fig. 3d), indicating better dispersion and distribution compared to the other samples. The evidence from the present studies implies that the Ag-SeO_2 nanoparticles are more stable in the aqueous solution medium than the Ag-TiO_2 nanoparticles. The Ag-TiO_2 nanoparticles possessed a larger hydrodynamic size and size distribution, which confirmed the aggregation of nanoparticles.[71] This is due to factors, including high surface energy, in the nanoparticles and "interparticle" attractive forces.[72] However, Ag-SeO_2 nanoparticles possessed a smaller hydrodynamic size and smaller size distribution, indicating better dispersion stability.[73]

The variation in the dispersion behavior of the two types of nanomaterials can be explained in terms of the surface chemistry of the nanoparticles, the type of capping agents, and the conditions of synthesis.[74] The nanoparticle aggregation together with stability exhibits signs of change owing to temperature effects, pH conditions, and exposure to light. Future investigations should focus on studying the storage behavior to understand completely the long-term stability performance of these nanocomposites in different environmental settings.

3.2.5. High-resolution transmission electron microscopy (HR-TEM). The HR-TEM image of the Ag-TiO_2 NC in Fig. 4a shows that the composite consists of spherical and irregularly shaped nanoparticles. The sizes vary with several particles having a clumped appearance. The morphology of the particles present in the sample, as well as the XRD data, indicates the formation of Ag-TiO_2 NC containing spherical and irregular-shaped particles. HR-TEM provides an opportunity for analysis at the nanoscale level and even separates particles and their lattice contrast. The lattice fringes enable the determination of the crystal structure and interplanar distance of the nanoparticles. Thus, from the lattice fringe patterns, the phase composition of the sample can be determined, such as anatase titanium dioxide and metallic silver.[67]

Generally, the HR-TEM image of Ag-SeO_2 NC (Fig. 4b) indicates that the samples display a non-uniform nature of mostly spherical and irregularly shaped nanoparticles. The size range of the particles is large, and some of them are aggregated. The observed presence of spherical and irregularly shaped particles confirms the synthesis of a composite material of silver and selenium dioxide nanoparticles. The HR-TEM images give a clear indication of well-dispersed Ag-TiO_2 and Ag-SeO_2 nanocomposites with a relatively narrow size distribution of the nanocomposites. The observed nanoparticles are spherical and have a relatively smooth surface.[13] The size distribution of the observed particles represents a relatively narrow size

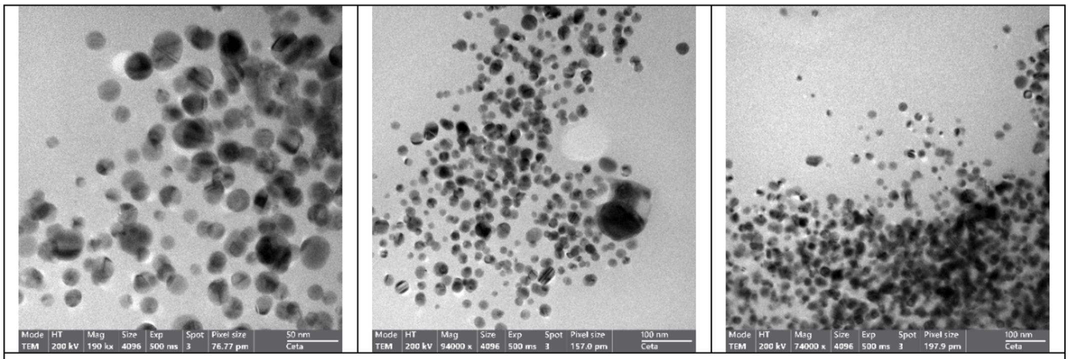

(a) Ag-TiO_2 NC

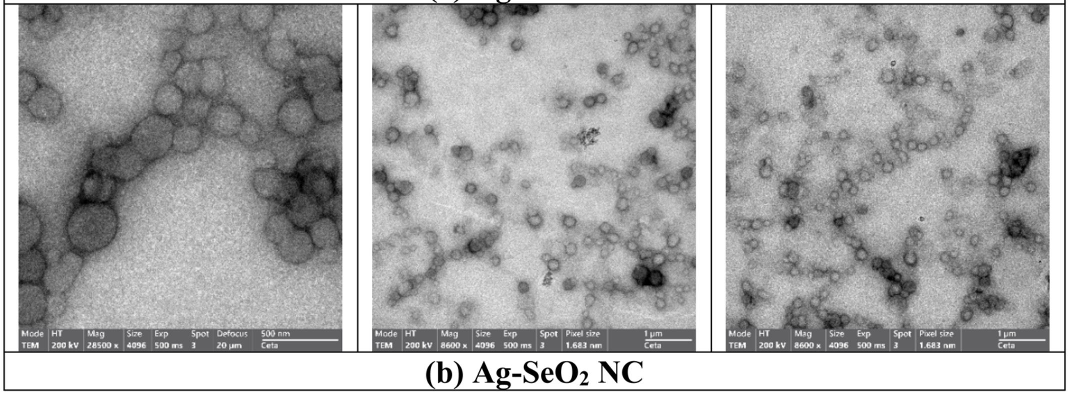

(b) Ag-SeO_2 NC

Fig. 4 HR-TEM images of (a) Ag-TiO_2 and (b) Ag-SeO_2 nanocomposites.

distribution, which improves the properties of the synthesized nanoparticles, such as catalytic properties and stability. This has been a result of the appropriate choice of capping agents during the synthesis process for the nanoparticles in question. The capping agents can also form a layer at the nanoparticle surface and thus reduce agglomeration and enhance stability.[15]

3.2.6. Energy-dispersive X-ray spectroscopy (EDX). EDX analysis was performed to confirm the elemental composition of the synthesized Ag-TiO_2 and Ag-SeO_2 nanomaterials. EDX analysis (Fig. 5 and Table S2†) confirmed the successful synthesis of both Ag-TiO_2 and Ag-SeO_2 nanomaterials.

For Ag-TiO_2 NC (Fig. 5a), the spectrum revealed the presence of carbon (16.13 wt%, 20.43 at%), oxygen (43.64 wt%, 52.53 at%), titanium (15.02 wt%, 16.01 at%), and silver (25.21 wt%, 12.03 at%). Similarly, for Ag-SeO_2 NC (Fig. 5b), the spectrum showed the presence of carbon (33.63 wt%, 45.29 at%), oxygen (28.50 wt%, 34.02 at%), selenium (12.63 wt%, 11.33 at%), and silver (25.24 wt%, 14.36 at%). The presence of these elements in the expected ratios confirms the successful incorporation of silver nanoparticles into the TiO_2 and SeO_2 matrices. The presence of carbon in both samples can be attributed to the use of organic capping agents during the synthesis process.[75] The capping agents help to stabilize the nanoparticles and prevent agglomeration.[76] However, the presence of carbon can also affect the properties of the nanomaterials, such as their surface area and catalytic activity.[77]

3.2.7. Scanning electron microscopy (SEM). The SEM image of Ag-TiO_2 NC (Fig. 6a) clearly shows the heterogeneous surface morphology with a cluster of particles having different sizes.

The nanoparticles have an inhomogeneous shape and porous structure that allows for increasing the material's surface and improves the catalytic or adsorbent properties. It is possible to form a composite nanomaterial with spherical and irregular-shaped particles, such as a combination of TiO_2 and silver nanoparticles. Aggregation is encountered often in nanoparticle synthesis and has a significant impact on the properties of the resulting materials, including the mass surface area, porosity, and catalytic activity.[78]

The SEM of Ag-SeO_2 NC (Fig. 6b) shows that the sample has irregular and rough surface morphology and agglomerated particles with sizeable variations in the size and shape of the NCs. The particles show a high level of irregularity in the surface structure, which may cause increased surface area and corresponding improvements in the catalytic or adsorptive material. However, owing to the porosity of the nanoparticles, there may be other active sites for interactions with target molecules or microorganisms.[79]

3.2.8. X-ray diffraction (XRD). By performing X-ray diffraction (XRD) on synthesized Ag-TiO_2 NCs, we determined the crystalline phases that existed, as illustrated in Fig. 7a and Table S3.† Analysis of this pattern identified the anatase TiO_2 phase according to JCPDS card no. 01-084-1286 and metallic silver through JCPDS card no. 00-001-1164. The successful production of the desired nanocomposite becomes evident through the detection of these phases in the analysis. The major

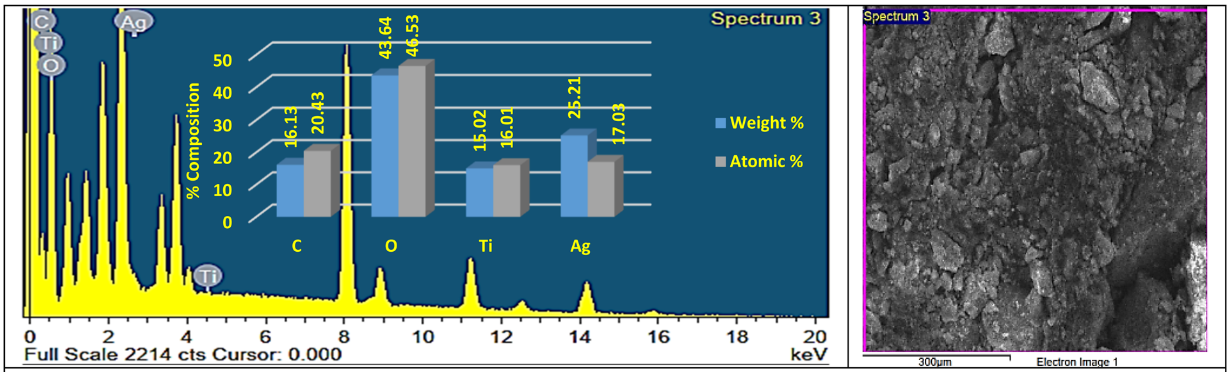

(a) Ag-TiO₂ NC

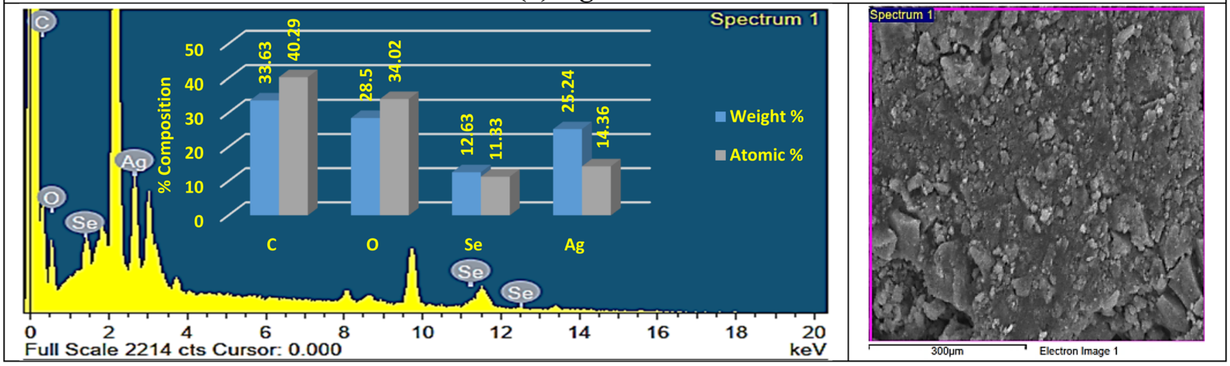

Fig. 5 EDX analysis of (a) Ag-TiO$_2$ and (b) Ag-SeO$_2$ nanocomposites.

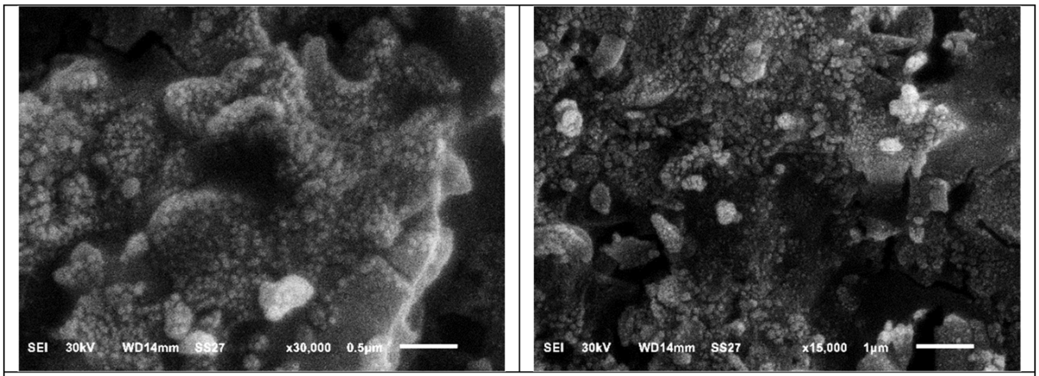

(a) Ag-TiO₂ NC

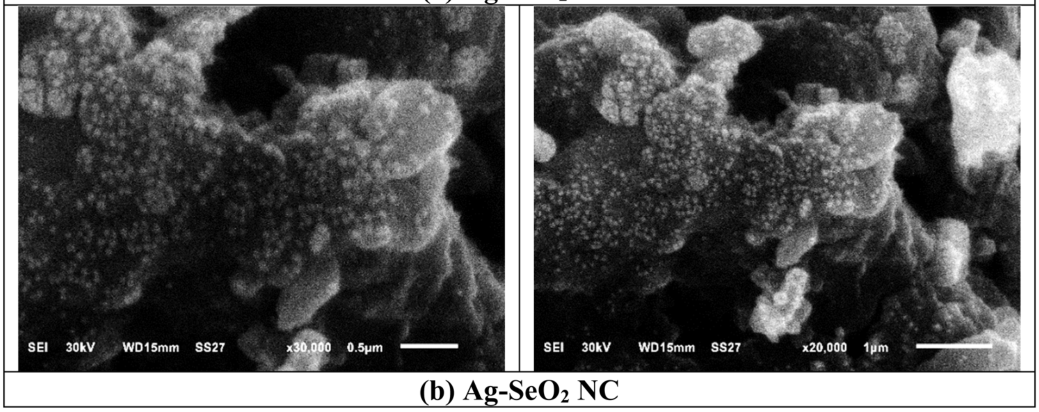

(b) Ag-SeO₂ NC

Fig. 6 SEM images of (a) Ag-TiO$_2$ and (b) Ag-SeO$_2$ nanocomposites.

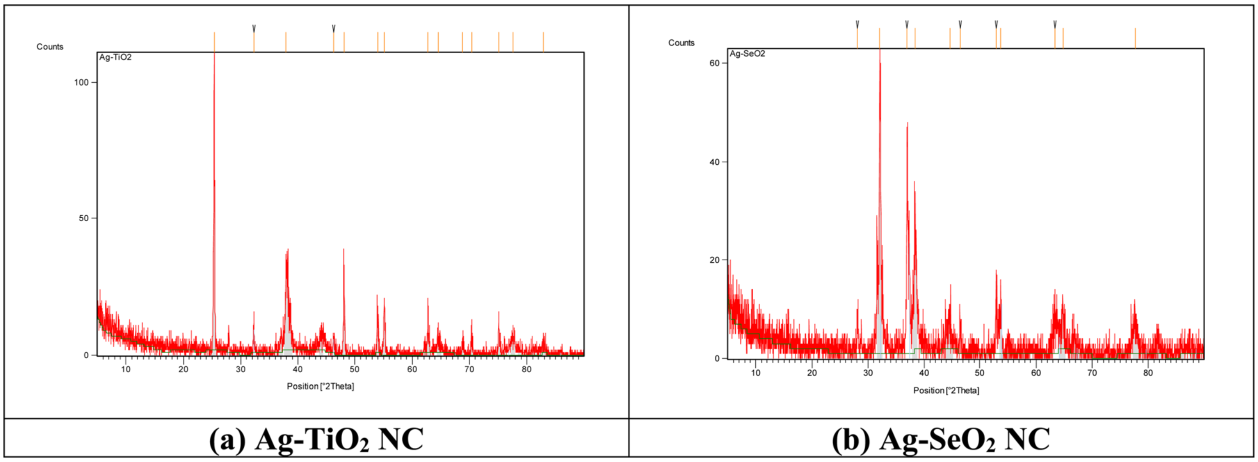

(a) Ag-TiO₂ NC

(b) Ag-SeO₂ NC

Fig. 7 XRD patterns of (a) Ag-TiO_2 and (b) Ag-SeO_2 nanocomposites.

XRD peaks observed at 25.37°, 37.91°, 48.09°, 53.96°, 55.16°, 62.73°, 68.79°, 70.41°, 75.11°, and 82.89° 2θ correspond to anatase TiO_2 characteristic diffractions. The 38.1° and 44.3° 2θ peaks originate from the silver metal present in the sample. The crystallite size of the anatase TiO_2 phase can be estimated through the application of the Scherrer equation. Rietveld refinement methods should be utilized to acquire exact measurements about the crystal structure and phase composition together with lattice parameter data. The crystallite size evaluation of the anatase TiO_2 phase requires the implementation of the Scherrer equation ($D = K\lambda/\beta \cos\theta$) using typical values of $K = 0.9$ and X-ray wavelength $\lambda = 1.5406$ Å for Cu Kα radiation, where β represents fractional maximum peak width in radians and θ represents Bragg angle. The crystallite size measurement of the anatase TiO_2 phase relies on applying the Scherrer equation to XRD-generated data. The material achieves enhanced reactivity and increased surface area because nanocrystalline TiO_2 formation produces small crystals.[80]

Scientists used XRD analysis to study the synthesized Ag-SeO_2 NCs illustrated in Fig. 7b and Table S5† for phase identification. The XRD pattern exhibited peaks that corresponded to the crystalline structures of silver selenide (Ag_2Se) with JCPDS card no. 01-087-0719 and selenium dioxide (SeO_2) with JCPDS card no. 01-085-0567. The successful production of Ag-SeO_2 NC material becomes evident through the detection of the identified phases in the synthesized structure. The prominent peaks at 32.06°, 38.37°, 44.67°, 53.70°, 64.83°, and 77.63° 2θ correspond to the characteristic diffraction peaks of silver selenide.[81] The additional peaks at 28.11°, 36.95°, 46.53°, and 63.43° 2θ can be attributed to the presence of selenium dioxide. The XRD analysis confirmed the successful synthesis of both Ag-TiO_2 and Ag-SeO_2 nanomaterials. The diffraction patterns exhibited characteristic peaks corresponding to the respective crystalline phases, indicating the formation of well-defined nanostructures.

3.3. Phytochemical analysis

The phytochemical analysis (Fig. 8 and Table S7†) revealed that *E. aphylla* extract and Ag-TiO_2 NC are rich sources of phenolic compounds, flavonoids, and tannins. For instance, *E. aphylla* extract contained 193.28 ± 1.73 mg gallic acid equivalent/g dry weight of phenolic compounds, 76.55 ± 1.48 mg catechin equivalent/g dry weight of flavonoids, and 123.8 ± 1.77 mg tannic acid equivalent/g dry weight of tannins. The phenolic compounds found in Ag-TiO_2 NC were 129.53 ± 1.09 gallic acid/g of dry weight, flavonoids were 66.19 ± 1.18 catechin/g dry weight and tannins were 90.2 ± 1.86 tannic acid/g dry weight. These compounds are known to have very high antioxidant activity. They can mop up free radicals, thus preventing cell injury from oxidative processes. Higher concentrations of these compounds in the *E. aphylla* extract and Ag-TiO_2 NC are attributed to their antioxidant effects. Ag-SeO_2 NC, although it contains comparatively lower concentrations of these bioactive compounds (82.889 ± 1.51 mg GAE/g DW of phenolic compounds, 17.89 ± 1.89 mg CE/g DW of flavonoids, and 28.83 ± 1.31 mg TAE/g DW of tannins), still possesses antioxidant features owing to the presence of silver nanoparticles. The capping agents of these nanoparticles can also act as electron donors and free radical scavengers, which may also make them antioxidants. These findings agree with earlier findings,[13,15,38,39] which established that phytochemical compounds are involved in the formation of nanoparticles and are thus depleted in the final nanocomposite.

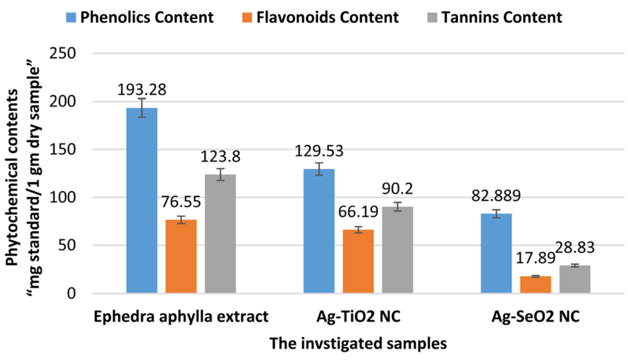

Fig. 8 Comparison of the phytochemical contents of the tested samples.

3.4. Antioxidant activity

The antioxidant activity of the *E. aphylla* extract and the nanomaterials was assessed by the DPPH assay using ascorbic acid as a standard. The results, as shown in Fig. 9a and Table S8,† verified that a lower IC_{50} value indicates higher antioxidant activity. Based on the results, *E. aphylla* extract and ascorbic acid exhibited the highest antioxidant activity, with IC_{50} values of 0.024 and 0.022 mg mL^{-1}, respectively. Ag-TiO_2 NC showed moderate antioxidant activity with an IC_{50} value of 0.044 mg mL^{-1}. The antioxidant activity in Ag-SeO_2 NC reached the lowest level when tested across all samples because they demonstrated an IC_{50} value of 0.092 mg mL^{-1}. The antioxidant properties of *E. aphylla* extract stem from multiple bioactive elements that contain flavonoids along with phenolic acids and alkaloids. The bioactive compounds in these substances give them the ability to neutralize free radicals by accepting electrons or donating hydrogen atoms, thus stopping oxidative destruction. Owing to their silver nanoparticle structure, Ag-TiO_2 and Ag-SeO_2 NCs demonstrate antioxidant functionality by functioning as electron donors that eliminate free radicals. Nanoparticles achieve higher antioxidant potential by utilizing their large surface area to facilitate more contact with free radicals.

The evaluation of *E. aphylla* extract and Ag-TiO_2 NC and Ag-SeO_2 NC antioxidant activity occurred through DPPH assay analysis. All the tested samples showed antioxidant activity that increased with higher concentrations, as illustrated in Fig. 9b. The DPPH scavenging activity of *E. aphylla* extract and ascorbic acid reached a maximum inhibition rate of over 80% when used at 0.094 and 0.06 mg mL^{-1}, respectively. Antioxidant properties were detected in Ag-TiO_2 NC and Ag-SeO_2 NCs, but these materials demonstrated reduced activity compared to *E. aphylla* plant extract and ascorbic acid. Under the study conditions, Ag-TiO_2 NC achieved a 79.25% inhibition rate at 0.13 mg mL^{-1} concentration while Ag-SeO_2 NC demonstrated 83.66% inhibition at 0.591 mg mL^{-1} concentration. *E. aphylla* extract exhibits antioxidant properties because it contains multiple bioactive compounds, including flavonoids, phenolic acids, and alkaloids. Both nanomaterials, Ag-TiO_2 and Ag-SeO_2 NCs, have antioxidant properties because silver nanoparticles in them function as electron donors and radical-scavenging agents.[82] The antioxidants found in nanoparticles become more effective owing to their extended surface areas, which increase free radical interactions.[83]

The results in this study concur with those reported by El-Zayat *et al.*,[8] highlighting the significant contribution of metal-based nanocomposites to antioxidant activity. Al-Barri *et al.*[84] investigated the antioxidant activity of *E. aphylla* and *Bassia muricata* extracts, confirming their high antioxidant capacity. These results were consistent with the results of this study, confirming *E. aphylla* extract as a strong antioxidant source. Ahmad *et al.*[85] prepared selenium-silver nanostructures and discovered enhanced antioxidant activity. Their findings are consistent with the results in this work concerning the results of Ag-SeO_2 NC. Alghonaim *et al.*[86] documented the antioxidant activity of Se@TiO_2 NPs embedded in biopolymers, which displayed high antioxidant activity. This is in concurrence with your research on Ag-TiO_2 NC, focusing on the free radical scavenging activity of silver and titanium dioxide nanoparticles. In short, the results in this research uphold the significant antioxidant activity of the *E. aphylla* extract and the moderate activity of both nanocomposites. Nanomaterials based on metals exhibit suitable potential for antioxidant usage, while their effectiveness depends on synthesis protocols and material compositions.

E. aphylla extract shows antioxidant activity because it contains different bioactive compounds, such as flavonoids, phenolic acids and alkaloids, according to ref. 8. Oxidative damage prevention occurs when these compounds provide either electrons or hydrogen atoms to neutralize free radicals.[87] Ag-TiO_2 and Ag-SeO_2 NCs demonstrate antioxidant activity because silver nanoparticles serve as electron donors that eliminate free radicals through their scavenging mechanism.[88]

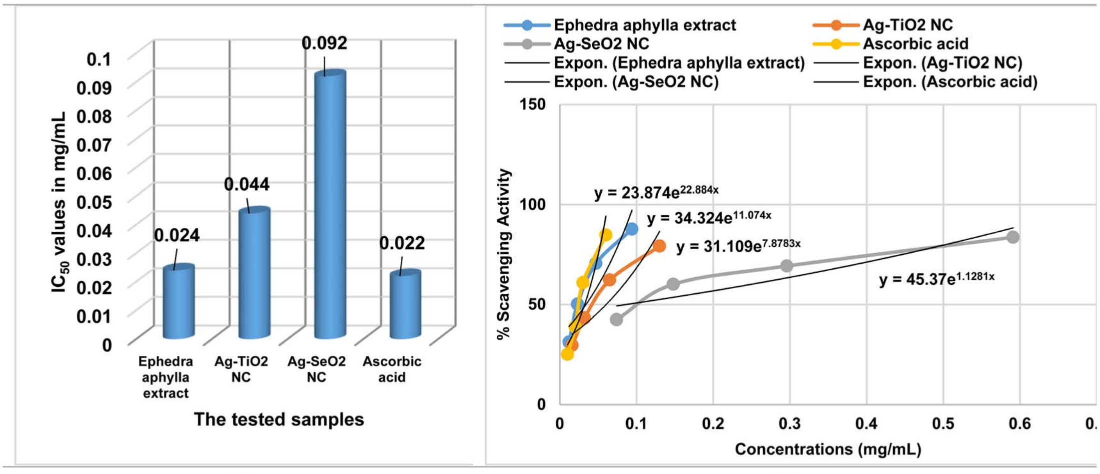

(a) (b)

Fig. 9 Antioxidant results using DPPH assay: (a) comparison of the antioxidant results expressed as IC_{50} in mg mL^{-1} of the investigated samples relative to the antioxidant standard. (b) Relationship between sample concentration (mg mL^{-1}) and % scavenging activity.

Nanoparticles possess enhanced free radical contact because of their enlarged surface area, which strengthens their antioxidant capabilities.[89] This study proves that *E. aphylla* extract and Ag-TiO_2 NC show high antioxidant capabilities.

3.5. Antimicrobial activity

3.5.1. Antibacterial activity. An evaluation of *E. aphylla* extract, Ag-TiO_2, and Ag-SeO_2 NC antibacterial activities against Gram-negative and Gram-positive bacteria occurred through disc diffusion experiments, as shown in Table 1 and Fig. 10. The antibacterial tests for *E. aphylla* extract, Ag-TiO_2 NC, and Ag-SeO_2 NC revealed no substantial inhibition of *E. coli*, regardless of the agent tested. The Ag-SeO_2 NC test discs created a zone of inhibition that reached 30.0 ± 1.20 mm, which matched the inhibition area made by the gentamicin standard (17.0 ± 1.29 mm). Two tested substances failed to inhibit the growth of *S. typhimurium* similar to their inadequate results against *E. coli*. The antibacterial performance of Ag-SeO_2 NC, as indicated by an inhibition zone of 30.0 ± 1.88 mm, surpassed the performance of gentamicin, which had a value of 14.0 ± 1.81 mm. Research findings indicated that the plant extract together with Ag-TiO_2 NC failed to demonstrate meaningful inhibitory effects against *E. cloacae*. The bacterial inhibition activities of Ag-SeO_2 NC revealed moderate results through the observation of an 11.0 ± 1.35 mm zone, while gentamicin produced similar inhibition results with a 14.0 ± 1.35 mm zone.

Both the plant extract and Ag-TiO_2 NC were ineffective against B. subtilis. Ag-SeO_2 NC displayed significant activity with a zone of 44.0 ± 1.09 mm, greatly surpassing the effectiveness of gentamicin (17.0 ± 1.41 mm). Ag-TiO_2 NC exhibited moderate activity against *B. cereus*, showing a zone of 14 mm, while Ag-SeO_2 NC presented a zone of 12.0 ± 1.16 mm, and gentamicin demonstrated better performance with a zone of 21.0 ± 1.56 mm. The plant extract showed moderate activity against *S. aureus*, achieving a zone of 17.0 ± 1.58 mm. Ag-TiO_2 NC and Ag-SeO_2 NC exhibited similar activity, with zones of 15.3 ± 1.06 mm and 31.0 ± 1.72 mm, respectively, while gentamicin revealed a zone of 15.0 ± 1.90 mm. The plant extract displayed moderate activity against *S. epidermidis*, yielding a zone of 12.0 ± 1.59 mm. Although Ag-TiO_2 NC was ineffective, Ag-SeO_2 NC showed a zone of 11.0 ± 1.34 mm. Gentamicin proved more effective with a zone of 17.0 ± 1.14 mm.

The observed antibacterial activity of Ag-SeO_2 NC can be attributed to its unique nanostructure and the synergistic effect of silver and selenium nanoparticles.[67] The high surface area of nanoparticles enhances their interaction with the bacterial cell wall and membrane, leading to disruption and cell death.[90–92] Silver nanoparticles are known to possess strong antimicrobial properties through their interaction with thiol groups in proteins and phospholipids, leading to membrane damage and cell death.[93,94] Selenium dioxide can induce oxidative stress in cells and interfere with essential cellular processes.[95] The combination of silver and selenium nanoparticles in Ag-SeO_2 NC enhanced the antimicrobial activity through a synergistic effect.

The antibacterial properties of the prepared nanocomposites in the current research were also compared with previously reported Ag-TiO_2, Ag-SeO_2 NCs, and selenium-based NPs. The results in this work showed promising inhibition against *S. aureus* and *B. cereus* comparable to Ag-TiO_2 NC (15.3 and 14 mm, respectively) and Ag-SeO_2 NC (31 and 12 mm, respectively).[96] The strong inhibition of *B. subtilis* by Ag-SeO_2 NC (44 mm) agrees with the enhanced antibacterial activity of selenium-based nanoparticles reported by Tran *et al.*[97] Similarly, *K. pneumonia* exhibited moderate inhibition (15.6 mm) against Ag-TiO_2 NC, while Ag-SeO_2 NC (31 mm) and previously studied selenium nanoparticles were more effective.[98,99] Against Gram-negative bacteria such as *E. typhimurium*, Ag-SeO_2 NC showed intense inhibition (30 mm), which is consistent with the superb antimicrobial potential of selenium nanoparticles observed in earlier research.[96,98] The data show the antimicrobial effectiveness of our nanocomposites against a wide range of bacteria.

However, the morphology of nanomaterials is crucial in determining their antimicrobial properties.[100] Antimicrobial action is based on numerous factors, including particle size, shape, surface area, and porosity.[101] Particles of smaller sizes are likely to be more antimicrobial in character owing to their greater surface area and hence more sites of microbial interaction.[102] Nanoparticles of spherical shape are likely to be

Table 1 Antibacterial activity results of *E. aphylla* extract and nanomaterials against various pathogenic bacteria

Microorganisms	Inhibition zones in mm			
	E. aphylla extract	Ag-TiO_2 NC	Ag-SeO_2 NC	Gentamycin
Gram-negative bacteria				
Escherichia coli (ATCC 10536)	−ve	−ve	30.0 ± 1.20	17.0 ± 1.29
Salmonella typhimurium (ATCC 25566)	−ve	−ve	30.0 ± 1.88	14.0 ± 1.81
Klebsiella pneumonia (ATCC 10031)	−ve	15.6 ± 1.43	31.0 ± 1.27	16.0 ± 1.03
Enterobacter cloacae (DMS 30054)	−ve	−ve	11.0 ± 1.35	14.0 ± 1.35
Gram-positive bacteria				
Bacillus subtilis (DMS 1088)	−ve	−ve	44.0 ± 1.09	17.0 ± 1.41
Bacillus cereus (EMCC number 1080)	−ve	14	12.0 ± 1.16	21.0 ± 1.56
Staphylococcus aureus (ATCC 6538)	17.0 ± 1.58	15.3 ± 1.06	31.0 ± 1.72	15.0 ± 1.90
Staphylococcus epidermidis (EMCC number 1353 [t])	12.0 ± 1.59	−ve	11.0 ± 1.34	17.0 ± 1.14

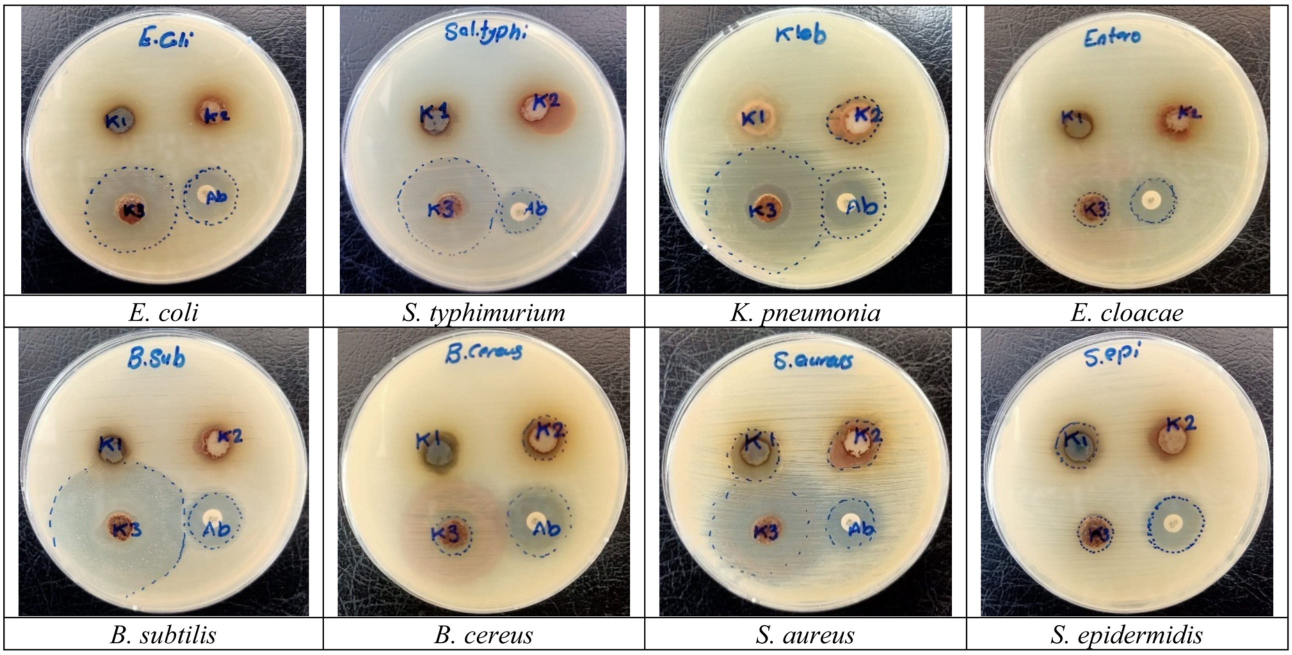

E. coli *S. typhimurium* *K. pneumonia* *E. cloacae*

B. subtilis *B. cereus* *S. aureus* *S. epidermidis*

Fig. 10 Images of Petri dishes that contain different bacterial pathogens and the tested samples. (K1) indicates the well inoculated with *E. aphylla* extract. (K2) indicates the well inoculated with Ag-TiO_2 NC. (K3) indicates the well inoculated with Ag-SeO_2 NC. (Ab) indicates the well inoculated with gentamycin.

characterized by good antimicrobial properties owing to their greater surface area and ease of penetrating cell membranes.[103] Rod-shaped nanoparticles are more active antimicrobials because they have pointed ends, which cause cell membranes to break more effectively.[104] Irregular shapes can generate more surface area and active sites, which can be utilized to enhance antimicrobial activity.[105] A greater surface area means more interaction with microorganisms, which also translates to more antimicrobial activity.[106] Porous structures can trap and kill microorganisms, which enhances antimicrobial activity.[107] The antimicrobial action of Ag-TiO_2 and Ag-SeO_2 nanomaterials is multifaceted and involves multiple parameters, such as the release of silver ions, the generation of ROS, and direct interaction with microbes. The results of this study show the potential of Ag-SeO_2 NC as a potent antibacterial agent. The optimization of the synthesis and formulation of Ag-SeO_2 NC should be further researched to achieve clinical efficacy.

Ag-TiO_2 and Ag-SeO_2 NCs use three distinct antibacterial mechanisms: ROS production, cell membrane penetration and intracellular damage. Bacterial cells induce silver (Ag^+) and selenium (Se^{2+}) ion release from these nanocomposites until the ions penetrate the cell membrane to disrupt microbial functions.[108] The production of reactive oxygen species (ROS) is enabled by TiO_2 under light exposure. Oxidative stress generates detrimental effects on bacterial cells, resulting in lipid peroxidation, protein oxidation, and DNA fragmentation, which causes bacterial cell death.[109] The ROS attacks bacterial cell membranes structurally while simultaneously time making membranes more permeable until the cells eventually rupture.[110] The antimicrobial activity of Ag-SeO_2 NC receives additional enhancement through its ability to block vital cellular processes and disrupt metabolic pathways.[13,67] The scope of ROS generation with ion release and membrane disruption events produces bacterial dysfunction and cell death, making these nanocomposites promising antimicrobial agents.

3.5.2. **Minimum inhibitory concentration (MIC).** The MIC values of the synthesized Ag-TiO_2 NCs and Ag-SeO_2 NCs against *S. aureus* and *K. pneumoniae* were determined using the broth dilution method (Table 2, Fig. S8 and Tables S9–S12†). The results indicate the lowest concentration of the nanocomposite required to inhibit the visible growth of the bacterial strains, in which a lower MIC value signifies higher antimicrobial activity. In this study, both nanocomposites exhibited significant antimicrobial activity against both bacterial species. However, Ag-SeO_2 NCs demonstrated superior antimicrobial activity, with lower MIC values compared to Ag-TiO_2 NCs.

Increased antimicrobial efficacy of Ag-SeO_2 NCs is due to the synergistic action between silver and selenium dioxide nanoparticles. Silver nanoparticles are strong antimicrobials owing to their interaction with the bacterial cell membrane, leading to

Table 2 MIC results of nanocomposites against *S. aureus* and *K. pneumonia* bacterial species

Sample	Bacterial species	Concentration ($mg\ mL^{-1}$)	$O.D_{600}$
Ag-TiO_2 NC	*S. aureus*	8.29	0.033
Ag-SeO_2 NC	*S. aureus*	0.2956	0.034
Ag-TiO_2 NC	*K. pneumonia*	4.145	0.050
Ag-SeO_2 NC	*K. pneumonia*	4.73	0.002

Table 3 Results of antifungal activity of the *E. aphylla* extract and nanomaterials against pathogenic fungal strains

	Inhibition zone diameter in mm of the tested samples		
Strains	*E. aphylla* extract	Ag-TiO_2 NC	Ag-SeO_2 NC
Candida glabrata	−ve	−ve	12
Aspergillus niger	−ve	−ve	12

damage and disruption.[111] Silver nanoparticles can also generate reactive oxygen species (ROS), which induce oxidative stress and cellular structure destruction.[112] Additionally, silver nanoparticles interfere with vital cell processes, such as DNA replication and protein synthesis.[113] Selenium dioxide (SeO_2), however, is a potent oxidant that can produce reactive oxygen species to impose oxidative stress on bacterial cells.[114] Reactive oxygen species can inflict damage on cell components, such as DNA, proteins, and lipids, which can lead to cell death in the long term.[115] The synergism of these two very active antimicrobial agents in Ag-SeO_2 NCs enhances their antimicrobial activity to a high extent, with decreased MIC values and higher efficacy against bacterial infection.

3.5.3. Antifungal activity. A disc diffusion assay was employed to evaluate the antifungal activity of *E. aphylla* extract, Ag-TiO_2 NC, and Ag-SeO_2 NC against *Candida glabrata* and *Aspergillus niger*. The results, summarized in Table 3 and Fig. 11, indicate that although the plant extract and Ag-TiO_2 NC exhibited no significant inhibitory activity, Ag-SeO_2 NC demonstrated promising antifungal efficacy against both fungal pathogens. The antifungal activity of Ag-SeO_2 NC noted can be attributed to the synergistic effect and nanostructure of the silver and selenium nanoparticles. Owing to the very large surface area, the nanoparticles can interact more with the cell wall and cell membrane of the fungus and can induce cell death and damage. Silver nanoparticles were found to possess very good antimicrobial activity. Ag NPs can interact with protein and phospholipid thiol groups, leading to membrane damage and fungal cell death.[116] Silver nanoparticles can also generate ROS, which can further induce oxidative stress and damage cellular structures.[117] Selenium dioxide, the second constituent of Ag-SeO_2 NC, is also antimicrobial in nature.[118] Selenium dioxide can induce oxidative stress in cells and interfere with vital cellular processes.[119] The synergistic effect of silver and selenium nanoparticles combined in Ag-SeO_2 NC can enhance the antimicrobial effect. The mechanisms of the antifungal effect of Ag-SeO_2 NC are unclear and should be further investigated. Overall, the results of this study indicate that Ag-SeO_2 NC is a promising antifungal agent.

3.6. Studying the mechanism of action of antifungal activity

3.6.1. FTIR spectroscopy. FTIR spectroscopy (Table 4) was utilized to investigate the potential interactions between the *C. glabrata* fungal cell wall components and the Ag-SeO_2 NC prepared. The FTIR spectrum of untreated *C. glabrata* (Fig. S9†) exhibited characteristic absorption bands for various functional groups, *i.e.*, O–H stretching vibrations at 3353 and 3273 cm^{-1}, C–H stretching vibrations at 2935 cm^{-1}, amide I band at 1674 cm^{-1}, amide II band at 1550 and 1516 cm^{-1}, and additional bands due to C–C, C–N, and C–O bonds. Following treatment with Ag-SeO_2 NC, the FTIR spectrum of *C glabrata* (Fig. S10†) underwent spectacular changes. New bands of absorption appeared at 1642 and 1579 cm^{-1}, which represent the formation of new C=N and C=C bonds, respectively. A new band emerged at 774 cm^{-1}, which represents the formation of metal–oxygen (M–O) bonds. These spectral changes confirm that the Ag-SeO_2 NC had interacted with the constituents of the fungal cell wall, leading to a shift in their structure and

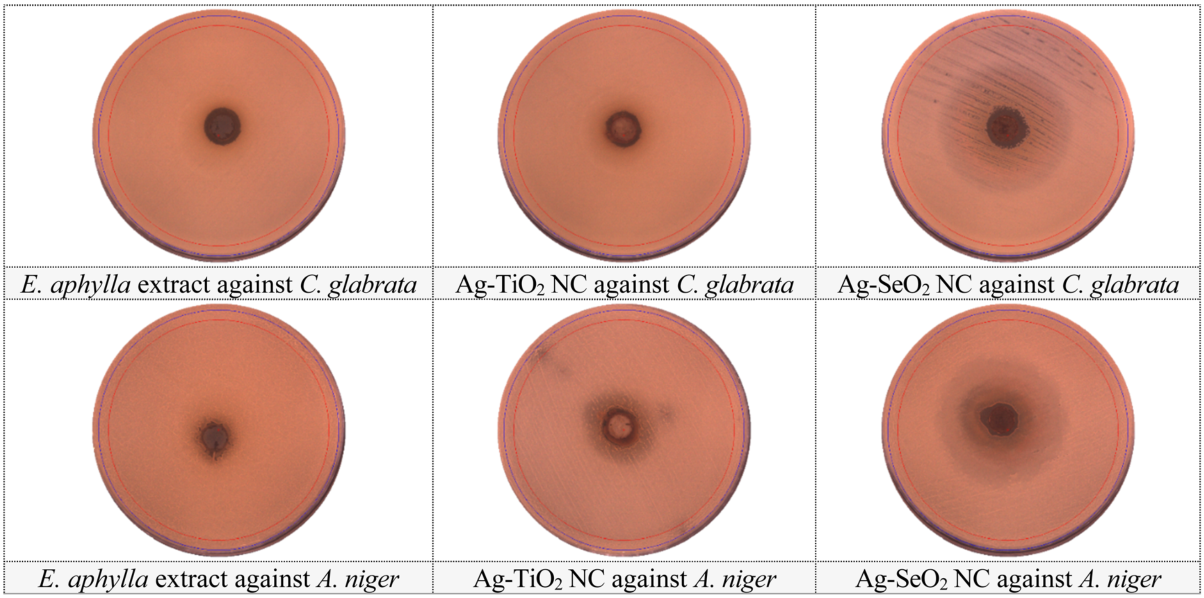
E. aphylla extract against *C. glabrata*
Ag-TiO_2 NC against *C. glabrata*
Ag-SeO_2 NC against *C. glabrata*
E. aphylla extract against *A. niger*
Ag-TiO_2 NC against *A. niger*
Ag-SeO_2 NC against *A. niger*

Fig. 11 Images of Petri dishes seeded with different pathogenic fungal strains and tested samples.

Table 4 FTIR analysis of treated and untreated fungal species with Ag-SeO_2 NC

Wavenumber (cm^{-1})	Untreated *C. glabrata*	Treated *C. glabrata*	Untreated *A. niger*	Treated *A. niger*	Functional group	Interpretation
3353–3526	3353, 3273	3366, 3276	3526, 3275	3365, 3275	O–H	O–H stretching vibration
2935–2968	2935	2933, 2873	2968, 2930, 2872	2934, 2873	C–H	C–H stretching vibration (aliphatic)
1674–1688	1674	1674, 1642, 1579	1688	1674, 1578	C=O	Amide I band (carbonyl stretching)
1550–1516	1550, 1516	1516	1503, 1452	1516, 1450	C–N	Amide II band (N–H bending and C–N stretching)
1452–1452	1452	1451	1452	1450	C–H	C–H bending vibration (methylene)
1405–1412	1405, 1398	1406, 1399	1412, 1385	1406, 1399	C–H	C–H bending vibration (methyl)
1308–1399	1308	1338, 1309	1236	1309, 1238	C–N	C–N stretching vibration
1238–1238	1238	1238	1236	1238	C–O	C–O stretching vibration (phenolic)
1120–1122	1120	1120	1122	1120	C–O	C–O stretching vibration (alcoholic)
1078–1078	1078	1078	1078	1079	C–O	C–O stretching vibration (alcoholic)
1037–1032	1037	1038	1032	1037	C–O	C–O stretching vibration (alcoholic)
981–990	981	990	979	923	C–H	C–H bending vibration (aromatic)
924–924	924	923	924	923	C–H	C–H bending vibration (aromatic)
851–850	851	850	849	850	C–H	C–H bending vibration (aromatic)
774–775		774	775	775	M–O	Metal–oxygen bond (Ag–O or Se–O)
653–400	530	530, 400	702, 653, 531, 398	425, 400	C–C, C–N, C–O	Skeletal vibrations

function.[120] The alterations observed in the FTIR spectra are good indications of the interaction between the Ag-SeO_2 NC and the cell wall of the fungus, which may be the reason for the antifungal activity of the nanoparticles.[121] Cell wall integrity disruption and new bond formation can lead to cell death and fungal growth inhibition. Similar to *C. glabrata*, the FTIR spectrum of untreated *A. niger* also displayed characteristic absorption bands for O–H stretching vibrations at 3526 and 3275 cm^{-1}; C–H stretching vibrations at 2968, 2930, and 2872 cm^{-1}; amide I band at 1688 cm^{-1}; and other bands for C–C, C–N, and C–O bonds (Fig. S11†). Following treatment with Ag-SeO_2 NC, there were significant changes in the FTIR spectrum of *A. niger* (Fig. S12†).

New absorption bands occurred at 1674 and 1578 cm^{-1}, corresponding to the existence of new C=N and C=C bonds, respectively. New absorption at 775 cm^{-1} also emerged, indicating the formation of metal–oxygen (M–O) bonds. The spectral changes prove that the Ag-SeO_2 NCs react with the constituents of the fungal cell wall, leading to structural and functional changes.[122] New bond formation and disruption of cell wall integrity may lead to cell death and inhibition of the growth of the fungus. The red shift of the O–H stretching band from 3526 cm^{-1} to 3365 cm^{-1} for treated *A. niger* verifies new hydrogen bond formation between the constituents of the fungal cell wall and Ag-SeO_2 NCs. This interaction further enhances the disruption of the cell wall structure and enhances the antifungal action of the nanoparticles.

3.6.2. HR-TEM.

The analysis of the HR-TEM images allowed for an understanding of the changes that occur in *C. glabrata* due to the presence of Ag-SeO_2 NC. The untreated *C. glabrata* cell control (Fig. 12a) appeared as round to oval-shaped cells with clear cell membranes and cell walls. The appearance of buds indicated an increase in such cells and presented signs that the cells were dividing. Nevertheless, on treatment with Ag-SeO_2 NC, substantial ultrastructure changes were observed (Fig. 12b). The treated cells exhibited strong signs of cell damage, such as cell wall rupture, membrane permeabilization, and leakage of the cytoplasm content. The cell wall, a vital structural molecule, was observed to be significantly weakened in many such treated cells with few cells showing a complete lack of cell wall. Similarly, the cell membrane, which acts as a primary structure for maintaining cellular equilibrium, was injured and altered in many of the cells. These disruptions affected the integrity of cytoplasmic compartmentalization and subsequently caused the release of cytoplasmic contents; cellular debris and electron-dense material were observed in the extracellular matrix.[123] These morphological changes can be attributed to the combined impact of Ag NPs and SeO_2 on the widespread structure of the TSH robot. The study also revealed that Ag NPs can penetrate cell membranes, causing membrane disruption and eventually membrane damage. They can also produce ROS, which results in oxidative stress and therefore impair various cellular constituents. Further, Ag NPs might possess toxic properties, which include the disruption of important cell functions, such as DNA synthesis and cell division.[116] SeO_2 is another compound that has an antimicrobial effect and can trigger oxidative stress in cells.[117] The current study shows that Ag NPs and SeO_2 combined in Ag-SeO_2 NC may have a synergistic effect on their antimicrobial activity, causing cell damage and suppression of fungal growth.

The analysis of the changes in the morphology of *A. niger* after exposure to tracer Ag-SeO_2 NCs is based on the data of the HR-TEM images. As presented in Fig. 12c, untreated *A. niger* presented a typical fungal morphology, including defined hyphae and clear cell walls. However, upon treatment with Ag-SeO_2 NC, the extent of cellular damage varied significantly. The treated fungal cells (Fig. 12d) revealed damage to the cell wall and cell membrane, the cytoplasm leaked, and the cells died.

The disruptions in the cell walls and membrane structure probably contributed to the disruption of cellular equilibrium

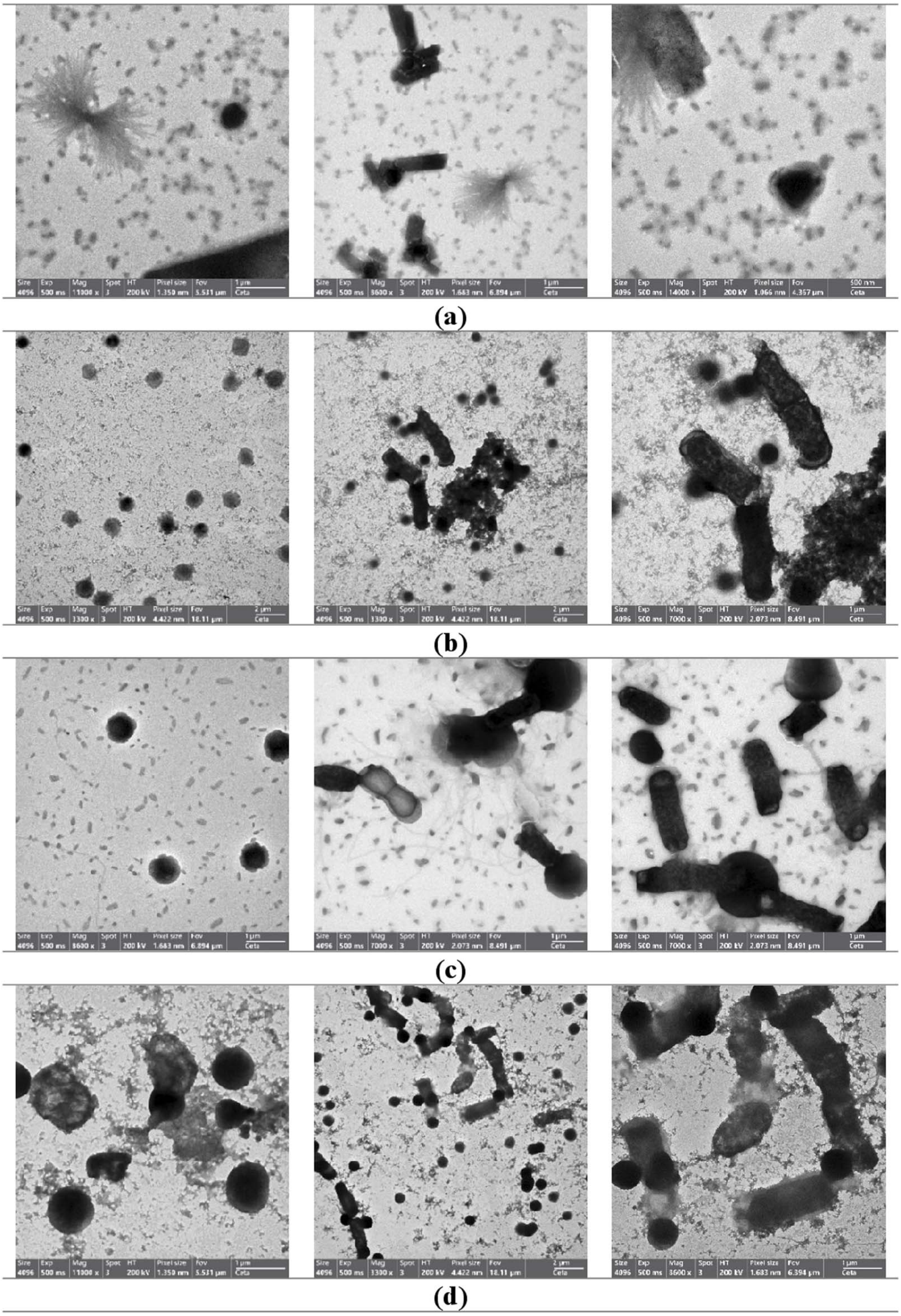

Fig. 12 The HR-TEM images of fungal pathogens treated and untreated with Ag-SeO_2 NC. (a) Presents *C. glabrata* untreated with Ag-SeO_2 NC. (b) Presents *C. glabrata* treated with Ag-SeO_2 NC. (c) Presents *A. niger* untreated with Ag-SeO_2 NC. (d) Presents *A. niger* treated with Ag-SeO_2 NC.

and prerequisite cellular processes. Possible factors that might have contributed to the anti-fungal activity of Ag-SeO_2 NC against *A. niger* may be summarized as follows: the silver nanoparticles (Ag NPs) could directly come into contact with the cell membrane, SMR damage, and cell membrane disruption.[116] They may also produce ROS, which causes cellular oxidative stress and leads to damage to cellular structures. Additionally, owing to their small size, Ag NPs can pose a threat to the cell's processes, including DNA replication and protein synthesis.[124] The selenium dioxide present in the nanocomposite may complement its antimicrobial activity through the imposition of oxidative stress. The combined effect of Ag NPs and SeO_2 in Ag-SeO_2 NCs probably increases the effectiveness of antimicrobial activity against *A. niger*. Through the synergistic action of the two effective antimicrobial components, Ag-SeO_2 NC could inhibit the growth of the fungal cell wall and membrane, leading to the cell death of the fungi.

4. Conclusion

This study provides an efficient and green protocol for the synthesis of Ag-TiO_2 and Ag-SeO_2 nanocomposites. The nanocomposites are well-characterized by different techniques, and the proposed mechanism for the formation of nanocomposites was investigated. UV-vis spectroscopy confirmed the presence of silver nanoparticles; FTIR spectroscopy indicated the involvement of plant extract biomolecules in the synthesis, and zeta potential analysis showed good colloidal stability. DLS analysis revealed differences in particle size distribution between the two nanomaterials. HR-TEM images visualized the morphology and particle size, while EDX analysis confirmed the elemental composition. SEM analysis showed the surface morphology and particle agglomeration. Finally, XRD analysis confirmed the crystalline phases present in the nanocomposites. The current study also provides valuable insights into the potential of natural and nanomaterial-based antimicrobial agents. *E. aphylla* extract and Ag-SeO_2 NC demonstrated significant antioxidant and antimicrobial activities, respectively. A high concentration of bioactive compounds in the plant extract, such as phenolic compounds, flavonoids, and tannins, explains the high antioxidant activity identified in this study. These compounds can reduce free radical concentrations and preserve the structure of cells from oxidative effects. The improvement in the antimicrobial properties of Ag-SeO_2 NC can be explained using the dual effect of the silver and selenium particles. Silver nanoparticles can encourage or impose membrane disruption and damage as a result of interactions with cells. They can also produce ROS, which, in turn, can cause oxidative stress and alter the cellular ultrastructure. Furthermore, it was found that silver nanoparticles can interfere with cell division and other operations, as basic as the protein synthesis process. Selenium dioxide is, in contrast, a powerful oxidative agent that may cause oxidative damage to cells through the production of ROS. Integrating these two highly effective antimicrobial agents in Ag-SeO_2 NC results in a composed enhanced antimicrobial effect. Characterization studies that involved FTIR spectroscopy coupled with HR-TEM imaging supported the working mechanism of Ag-SeO_2 NC. From the obtained FTIR spectra, it can be observed that there are considerable changes in the functional groups of the fungal cell wall of the treated cells with Ag-SeO_2 NC that pointed towards interaction and possible disruption of the cell wall. The analysis of the HR-TEM images of *C. glabrata* and *A. niger* cells after interaction with Ag-SeO_2 NC revealed cell damage demonstrated by cell wall deformation, membrane disorganization, and cytoplasmic leakage. All these results add more evidence to the belief that Ag-SeO_2 NC could be a potential material for use as a broad-spectrum antimicrobial agent. Subsequent studies, which will examine these mechanisms of action in greater depth, could supply useful information in creating new classes of antimicrobial agents.

Data availability

The data supporting the findings of this study are available in the ESI† file and can also be obtained from the corresponding author upon reasonable request.

Conflicts of interest

No conflict of interest was declared by the authors.

Acknowledgements

This work is not funded by any funding agencies.

References

1 D. Chinemerem Nwobodo, M. C. Ugwu, C. Oliseloke Anie, M. T. Al-Ouqaili, J. Chinedu Ikem, U. Victor Chigozie and M. Saki, *J. Clin. Lab. Anal.*, 2022, **36**, e24655.
2 S. Mickymaray, *Antibiotics*, 2019, **8**, 257.
3 M. T. El-Saadony, N. M. Zabermawi, N. M. Zabermawi, M. A. Burollus, M. E. Shafi, M. Alagawany, N. Yehia, A. M. Askar, S. A. Alsafy, A. E. Noreldin and A. F. Khafaga, *Food Rev. Int.*, 2023, **39**, 2138–2160.
4 D. E. González-Juárez, A. Escobedo-Moratilla, J. Flores, S. Hidalgo-Figueroa, N. Martínez-Tagüeña, J. Morales-Jiménez, A. Muñiz-Ramírez, G. Pastor-Palacios, S. Pérez-Miranda, A. Ramírez-Hernández and J. Trujillo, *Molecules*, 2020, **25**, 3283.
5 A. S. Dousari, N. Satarzadeh, B. Amirheidari and H. Forootanfar, *Rev. Bras. Farmacogn.*, 2022, **32**, 883–899.
6 M. Kumar, P. Kumar, A. Kaur, S. Kaur and S. Kaur, *Thai J. Pharm. Sci.*, 2024, **47**, 7.
7 W. Al-Awaida, B. J. Al-Hourani, M. Akash, W. H. Talib, S. Zein, R. R. Falah and Z. Aburubaiha, *J. Cancer Res. Ther.*, 2018, **14**, 1350–1354.
8 M. M. El-Zayat, M. M. Eraqi, H. Alrefai, A. Y. El-Khateeb, M. A. Ibrahim, H. M. Aljohani, M. M. Aljohani and M. M. Elshaer, *Biomolecules*, 2021, **11**, 470, DOI: 10.3390/biom11030470.
9 M. Ashour, A. T. Mansour, A. M. Abdelwahab and A. E. Alprol, *Processes*, 2023, **11**, 3356.
10 E. O. Ogunsona, R. Muthuraj, E. Ojogbo, O. Valerio and T. H. Mekonnen, *Appl. Mater. Today*, 2020, **18**, 100473.
11 A. Raghunath and E. Perumal, *Int. J. Antimicrob. Agents*, 2017, **49**, 137–152.
12 S. Ying, Z. Guan, P. C. Ofoegbu, P. Clubb, C. Rico, F. He and J. Hong, *Environ. Technol. Innovation*, 2022, **26**, 102336.
13 K. M. Elattar, F. O. Al-Otibi, M. S. El-Hersh, A. A. Attia, N. M. Eldadamony, A. Elsayed, F. Menaa and W. I. Saber, *Heliyon*, 2024, **10**, e28359.

14 Y. A. Hameed, A. Almahri, A. I. Alalawy, S. F. Ibarhiam, N. D. Alkhathami, H. Mattar, W. M. Alamoudi and N. M. El-Metwaly, *Inorg. Chim. Acta*, 2025, **574**, 122390.

15 K. M. Elattar, A. A. Ghoniem, F. O. Al-Otibi, M. S. El-Hersh, Y. A. Helmy and W. I. Saber, *Appl. Sci.*, 2023, **13**, 10110.

16 P. Ribao, J. Corredor, M. J. Rivero and I. Ortiz, *J. Hazard. Mater.*, 2019, **372**, 45–51.

17 Y. Gu, J. Dong, J. Li, Q. Luo, X. Dong, G. Tang, J. Zhang, X. Du, Q. Pu, L. He and K. Zhao, *Front. Vet. Sci.*, 2023, **10**, 1121082.

18 A. Chwalibog, E. Sawosz, A. Hotowy, J. Szeliga, S. Mitura, K. Mitura, M. Grodzik, P. Orlowski and A. Sokolowska, *Int. J. Nanomed.*, 2010, **5**, 1085–1094.

19 M. Alavi and N. Karimi, *Artif. Cells, Nanomed., Biotechnol.*, 2018, **46**, 399–413.

20 G. R. Khalaf, K. N. Abbas and A. M. Abbas, *Braz. J. Phys.*, 2024, **54**, 75.

21 M. Jariyaboon, P. Masrinoul, J. Komaikul, K. Muenkaew, S. Juntarapornchai, K. Ketsuwan, E. Rodpai, S. Ruangdachsuwan, S. Palabodeewat and C. Chitichotpanya, *Emergent Mater.*, 2023, **6**, 1259–1272.

22 S. Kang, J. Choi, G. Y. Park, H. R. Kim and J. Hwang, *Appl. Surf. Sci.*, 2022, **599**, 153930.

23 M. M. Abutalib and A. J. P. T. Rajeh, *Polym. Test.*, 2021, **93**, 107013.

24 C. Liu, L. Geng, Y. Yu, Y. Zhang, B. Zhao and Q. Zhao, *Biofouling*, 2018, **34**, 190–199.

25 M. M. Rashid, B. Tomšič, B. Simončič, I. Jerman, D. Štular and M. Zorc, *Appl. Surf. Sci.*, 2022, **595**, 153521.

26 L. Juan, Z. Zhimin, M. Anchun, L. Lei and Z. Jingchao, *Int. J. Nanomed.*, 2010, **5**, 261–267.

27 A. García, L. Delgado, J. A. Torà, E. Casals, E. González, V. Puntes, X. Font, J. Carrera and A. Sánchez, *J. Hazard. Mater.*, 2012, **199**, 64–72.

28 N. El-Gazzar and A. M. Ismail, *Biocatal. Agric. Biotechnol.*, 2020, **27**, 101708.

29 K. Staats, M. Pilz, J. Sun, T. Boiadjieva-Scherzer, H. Kronberger, S. Tobudic, R. Windhager and J. Holinka, *Sci. Rep.*, 2022, **12**, 8298.

30 G. M. Khiralla and B. A. El-Deeb, *LWT–Food Sci. Technol.*, 2015, **63**, 1001–1007.

31 E. Zonaro, S. Lampis, R. J. Turner, S. J. S. Qazi and G. Vallini, *Front. Microbiol.*, 2015, **6**, 584.

32 M. Darroudi, A. Rangrazi, K. Ghazvini, H. Bagheri and A. Boruziniat, *Pesqui. Bras. Odontopediatr. Clin. Integr.*, 2021, **21**, e0121.

33 Y. Guo, C. Cheng, J. Wang, Z. Wang, X. Jin, K. Li, P. Kang and J. Gao, *J. Hazard. Mater.*, 2011, **192**, 786–793.

34 M. Skiba and V. Vorobyova, *Appl. Nanosci.*, 2023, **13**, 5185–5198.

35 F. Ahmed, D. Zhang, X. Tang and P. K. Malakar, *Foods*, 2024, **13**, 4026.

36 M. Surya, S. Sampath, S. B. Vairamuthu, P. G. Sravanthy, B. Ramachandran, M. M. Al-Ansari, T. Asmelash and M. Saravanan, *Mater. Technol.*, 2024, **39**, 2331899.

37 A. A. Ghoniem, K. M. Elattar, A. S. Alotaibi, H. Ghabban, M. S. El Hersh, A. Y. El-Khateeb, Y. A. El-Amier, H. M. El-Gendy, N. M. Eldadamony, W. I. Saber and A. Elsayed, *Eur. J. Plant Pathol.*, 2024, **170**, 567–591.

38 A. A. Alanazi, W. I. Saber, M. A. AlDamen and K. M. Elattar, *Int. J. Biol. Macromol.*, 2024, **280**, 135862.

39 M. M. Hammouda, A. A. Alanazi and K. M. Elattar, *ChemistrySelect*, 2024, **9**, e202401385.

40 M. E. Mert, B. D. Mert and K. M. Elattar, *ChemistrySelect*, 2025, **10**, e202403151.

41 M. Platzer, S. Kiese, T. Herfellner, U. Schweiggert-Weisz and P. Eisner, *Antioxidants*, 2021, **10**, 811.

42 A. M. Shraim, T. A. Ahmed, M. M. Rahman and Y. M. Hijji, *LWT–Food Sci. Technol.*, 2021, **150**, 111932.

43 S. Perumalla and N. Nayeem, *Int. J. Phytother. Res.*, 2012, **2**, 16–19.

44 İ. Gulcin and S. H. Alwasel, *Processes*, 2023, **11**, 2248.

45 M. Asadujjaman, M. A. Hossain and U. K. Karmakar, *Pharmacologyonline*, 2013, **1**, 161–165.

46 B. Athanassiadis, P. V. Abbott, N. George and L. J. Walsh, *Aust. Dent. J.*, 2009, **54**, 141–146.

47 M. A. Islam, M. M. Alam, M. E. Choudhury, N. Kobayashi and M. U. Ahmed, *Bangladesh J. Vet. Med.*, 2008, **6**, 121–126.

48 R. Dabur, H. Singh, A. K. Chhillar, M. Ali and G. L. Sharma, *Fitoterapia*, 2004, **75**, 389–391.

49 M. A. Sobi, M. R. Bindhu, D. Usha, R. Rajagopal, A. Alfarhan, S. Arokiyaraj and M. Umadevi, *J. Cryst. Growth*, 2024, **637**, 127708.

50 V. K. Sharma, C. M. Sayes, B. Guo, S. Pillai, J. G. Parsons, C. Wang, B. Yan and X. Ma, *Sci. Total Environ.*, 2019, **653**, 1042–1051.

51 S. T. Kochuveedu, Y. H. Jang and D. H. Kim, *Chem. Soc. Rev.*, 2013, **42**(21), 8467–8493.

52 M. M. Abutalib and A. Rajeh, *Phys. B*, 2020, **578**, 411796.

53 S. M. Amini, *Mater. Sci. Eng., C*, 2019, **103**, 109809.

54 A. Barhoum, J. Jeevanandam, A. Rastogi, P. Samyn, Y. Boluk, A. Dufresne, M. K. Danquah and M. Bechelany, *Nanoscale*, 2020, **12**, 22845–22890.

55 A. Albanese, P. S. Tang and W. C. Chan, *Annu. Rev. Biomed. Eng.*, 2012, **14**, 1–16.

56 F. Dumur, A. Guerlin, E. Dumas, D. Bertin, D. Gigmes and C. R. Mayer, *Gold Bull.*, 2011, **44**, 119–137.

57 V. S. Sousa and M. R. Teixeira, *Environ. Chem.*, 2013, **10**(4), 313–322.

58 H. P. Nagaiah, M. B. Samsudeen, A. R. Augustus and K. P. Shunmugiah, *Discover Nano*, 2025, **20**, 14.

59 S. Shrestha, B. Wang and P. Dutta, *Adv. Colloid Interface Sci.*, 2020, **279**, 102162.

60 C. N. Dipunadas and V. B. Jothy, *J. King Saud Univ., Sci.*, 2019, **31**, 372–383.

61 V. Sharma, D. Verma and G. S. Okram, *J. Phys.: Condens. Matter*, 2020, **32**, 145302.

62 C. S. Seney, B. M. Gutzman and R. H. Goddard, *J. Phys. Chem. C*, 2009, **113**, 74–80.

63 H. T. Liao and C. S. Wu, *J. Polym. Sci., Part B: Polym. Phys.*, 2004, **42**, 4272–4280.

64 T. Ivanova, A. Harizanova, T. Koutzarova and R. Closset, *Molecules*, 2024, **29**, 5156.

65 N. Nazar, I. Bibi, S. Kamal, M. Iqbal, S. Nouren, K. Jilani, M. Umair and S. Ata, *Int. J. Biol. Macromol.*, 2018, **106**, 1203–1210.
66 A. Bachvarova-Nedelcheva, R. Iordanova, K. L. Kostov, V. Ganev and Y. Dimitriev, *J. Non-Cryst. Solids*, 2018, **481**, 138–147.
67 A. A. Ghoniem, K. M. Elattar, F. O. Al-Otibi, A. Elsayed, M. S. El-Hersh, A. Y. El-Khateeb, Y. A. Helmy and W. I. Saber, *RSC Adv.*, 2024, **14**, 7088–7111.
68 E. Illés and E. Tombácz, *Colloids Surf., A*, 2003, **230**, 99–109.
69 J. Jiang, G. Oberdörster and P. Biswas, *J. Nanopart. Res.*, 2009, **11**, 77–89.
70 A. Serrano-Lotina, R. Portela, P. Baeza, V. Alcolea-Rodríguez, M. Villarroel and P. Ávila, *Catal. Today*, 2023, **423**, 113862.
71 J. M. Zook, V. Rastogi, R. I. MacCuspie, A. M. Keene and J. Fagan, *ACS Nano*, 2011, **5**, 8070–8079.
72 Y. Min, M. Akbulut, K. Kristiansen, Y. Golan and J. Israelachvili, *Nat. Mater.*, 2008, **7**, 527–538.
73 B. Krause, M. Mende, P. Pötschke and G. Petzold, *Carbon*, 2010, **48**, 2746–2754.
74 C. M. Phan and H. M. Nguyen, *J. Phys. Chem. A*, 2017, **121**, 3213–3219.
75 N. M. Eldadamony, A. A. Ghoniem, A. A. Al-Askar, A. A. Attia, M. S. El-Hersh, K. M. Elattar, H. Alrdahi and W. I. Saber, *Int. J. Biol. Macromol.*, 2024, **269**, 132109.
76 M. M. Hammouda, K. Shalabi, A. A. Alanazi, K. M. Elattar, M. A. Azzam and M. M. Rashed, *RSC Adv.*, 2023, **13**, 32532–32546.
77 J. Zhu, A. Holmen and D. Chen, *ChemCatChem*, 2013, **5**, 378–401.
78 E. Antolini, *Appl. Catal., B*, 2016, **181**, 298–313.
79 Q. Mu, G. Jiang, L. Chen, H. Zhou, D. Fourches, A. Tropsha and B. Yan, *Chem. Rev.*, 2014, **114**, 7740–7781.
80 M. S. Hossain and S. Ahmed, *Results Mater.*, 2023, **20**, 100492.
81 D. A. García, L. Mendoza, K. Vizuete, A. Debut, M. T. Arias, A. Gavilanes, T. Terencio, E. Ávila, C. Jeffryes and S. A. Dahoumane, *Molecules*, 2020, **25**(21), 5193.
82 Z. Bedlovičová, I. Strapáč, M. Baláž and A. Salayová, *Molecules*, 2020, **25**, 3191.
83 M. Misawa and J. Takahashi, *Nanomed. Nanotechnol. Biol. Med.*, 2011, **7**, 604–614.
84 S. N. Al-Barri, T. M. Al-Deeb, A. T. Al-Fawwaz, M. M. Al-Omari and K. M. Al-Qaoud, *Plant Cell Biotechnol. Mol. Biol.*, 2021, **22**, 47–64.
85 W. Ahmad, S. Shams, A. Ahmad, Y. Wei, Q. Yuan, A. U. Khan, M. S. Khan, A. Ur Rahman and M. Iqbal, *Appl. Nanosci.*, 2020, **10**, 1191–1204.
86 M. I. Alghonaim, S. A. Alsalamah, A. M. Mohammad and T. M. Abdelghany, *Biomass Convers. Biorefin.*, 2025, **15**, 6767–6779.
87 G. A. Engwa, *Free Radicals and the Role of Plant Phytochemicals as Antioxidants against Oxidative Stress-Related Diseases, Phytochemicals: Source of Antioxidants and Role in Disease Prevention*, BoD–Books on Demand, 2018, vol. 7, pp. 49–74.
88 S. Firoozi, M. Jamzad and M. Yari, *J. Nanostruct. Chem.*, 2016, **6**, 357–364.
89 Z. Nie, K. J. Liu, C. J. Zhong, L. F. Wang, Y. Yang, Q. Tian and Y. Liu, *Free Radicals Biol. Med.*, 2007, **43**, 1243–1254.
90 B. Ramalingam, T. Parandhaman and S. K. Das, *ACS Appl. Mater. Interfaces*, 2016, **8**, 4963–4976.
91 M. A. Ansari, H. M. Khan, A. A. Khan, M. K. Ahmad, A. A. Mahdi, R. Pal and S. S. Cameotra, *J. Basic Microbiol.*, 2014, **54**, 905–915.
92 A. Ahmad, Y. Wei, F. Syed, K. Tahir, A. U. Rehman, A. Khan, S. Ullah and Q. Yuan, *Microb. Pathog.*, 2017, **102**, 133–142.
93 A. S. Joshi, P. Singh and I. Mijakovic, *Int. J. Mol. Sci.*, 2020, **21**, 7658.
94 A. Roy, O. Bulut, S. Some, A. K. Mandal and M. D. Yilmaz, *RSC Adv.*, 2019, **9**, 2673–2702.
95 M. Bébien, G. Lagniel, J. Garin, D. Touati, A. Verméglio and J. Labarre, *J. Bacteriol.*, 2002, **184**, 1556–1564.
96 O. Bilek, Z. Fohlerova and J. Hubalek, *PLoS One*, 2019, **14**, e0214066.
97 P. A. Tran, N. O'Brien-Simpson, J. A. Palmer, N. Bock, E. C. Reynolds, T. J. Webster, A. Deva, W. A. Morrison and A. J. O'Connor, *Int. J. Nanomed.*, 2019, **14**, 4613–4624.
98 L. D. Geoffrion, T. Hesabizadeh, D. Medina-Cruz, M. Kusper, P. Taylor, A. Vernet-Crua, J. Chen, A. Ajo, T. J. Webster and G. Guisbiers, *ACS Omega*, 2020, **5**, 2660–2669.
99 Q. Wang, L. M. Barnes, K. I. Maslakov, C. A. Howell, M. J. Illsley, P. Dyer and I. N. Savina, *Mater. Sci. Eng., C*, 2021, **121**, 111859.
100 R. Kumar, A. Umar, G. Kumar and H. S. Nalwa, *Ceram. Int.*, 2017, **43**, 3940–3961.
101 J. Sawai, H. Igarashi, A. Hashimoto, T. Kokugan and M. Shimizu, *J. Chem. Eng. Jpn.*, 1996, **29**, 251–256.
102 B. Lallo da Silva, M. P. Abuçafy, E. Berbel Manaia, J. A. Oshiro Junior, B. G. Chiari-Andréo, R. C. R. Pietro and L. A. Chiavacci, *Int. J. Nanomed.*, 2019, **14**, 9395–9410.
103 M. Inam, J. C. Foster, J. Gao, Y. Hong, J. Du, A. P. Dove and R. K. O'Reilly, *J. Polym. Sci., Part A: Polym. Chem.*, 2019, **57**, 255–259.
104 F. A. Z. Sayed, N. G. Eissa, Y. Shen, D. A. Hunstad, K. L. Wooley and M. Elsabahy, *J. Nanobiotechnol.*, 2022, **20**, 536.
105 B. Abebe, E. A. Zereffa, A. Tadesse and H. A. Murthy, *Nanoscale Res. Lett.*, 2020, **15**, 1–19.
106 R. Kaur and S. Liu, *Prog. Surf. Sci.*, 2016, **91**, 136–153.
107 T. M. S. U. Gunathilake, Y. C. Ching, K. Y. Ching, C. H. Chuah and L. C. Abdullah, *Polymers*, 2017, **9**, 160.
108 N. F. Fahmy, M. M. Abdel-Kareem, H. A. Ahmed, M. Z. Helmy and E. A. R. Mahmoud, *Microb. Cell Fact.*, 2025, **24**, 6.
109 V. I. Lushchak, Oxidative stress and mechanisms of protection against it in bacteria, *Biochemistry*, 2001, **66**, 476–489.
110 T. Y. Wang, M. D. J. Libardo, A. M. Angeles-Boza and J. P. Pellois, *ACS Chem. Biol.*, 2017, **12**, 1170–1182.
111 B. Ahmed, A. Hashmi, M. S. Khan and J. Musarrat, *Adv. Powder Technol.*, 2018, **29**, 1601–1616.

112 Y. H. Lee, F. Y. Cheng, H. W. Chiu, J. C. Tsai, C. Y. Fang, C. W. Chen and Y. J. Wang, *Biomaterials*, 2014, **35**, 4706–4715.

113 P. V. AshaRani, S. Sethu, H. K. Lim, G. Balaji, S. Valiyaveettil and M. P. Hande, *Genome Integr.*, 2012, **3**, 1–14.

114 P. S. Bapte, S. S. Pansambal and S. Borgave, *J. Nanostruct.*, 2022, **12**, 178–193.

115 C. A. Juan, J. M. Pérez de la Lastra, F. J. Plou and E. Pérez-Lebeña, *Int. J. Mol. Sci.*, 2021, **22**, 4642.

116 L. Wang, L. Liu and X. Zhou, *Food Bioprocess Technol.*, 2024, **17**, 2304–2325.

117 Y. H. Lee, F. Y. Cheng, H. W. Chiu, J. C. Tsai, C. Y. Fang, C. W. Chen and Y. J. Wang, *Biomaterials*, 2014, **35**, 4706–4715.

118 N. Filipović, D. Ušjak, M. T. Milenković, K. Zheng, L. Liverani, A. R. Boccaccini and M. M. Stevanović, *Front. Bioeng. Biotechnol.*, 2021, **8**, 624621.

119 Y. Xiao, X. Zhang and Q. Huang, *Int. J. Biol. Macromol.*, 2022, **213**, 339–351.

120 R. M. Elamawi, R. E. Al-Harbi and A. A. Hendi, *Egypt. J. Biol. Pest Control*, 2018, **28**, 1–11.

121 P. Kanhed, S. Birla, S. Gaikwad, A. Gade, A. B. Seabra, O. Rubilar, N. Duran and M. Rai, *Mater. Lett.*, 2014, **115**, 13–17.

122 F. Faghihzadeh, N. M. Anaya, L. A. Schifman and V. Oyanedel-Craver, *Nanotechnol. Environ. Eng.*, 2016, **1**, 1–16.

123 M. A. Wallig and E. B. Janovitz, Morphologic manifestations of toxic cell injury, in *Haschek and Rousseaux's Handbook of Toxicologic Pathology*, Academic Press, 2022, pp. 113–148.

124 L. Wei, J. Lu, H. Xu, A. Patel, Z. S. Chen and G. Chen, *Drug Discovery Today*, 2015, **20**, 595–601.